

Durham Research Online

Deposited in DRO:

03 January 2014

Version of attached file:

Published Version

Peer-review status of attached file:

Peer-reviewed

Citation for published item:

Lehmer, B.D. and Alexander, D.M. and Bauer, F.E. and Brandt, W.N. and Goulding, A.D. and Jenkins, L.P. and Ptak, A. and Roberts, T.P. (2010) 'A Chandra perspective on galaxy-wide X-ray binary emission and its correlation with star formation rate and stellar mass : new results from luminous infrared galaxies.', *Astrophysical journal.*, 724 (1). pp. 559-571.

Further information on publisher's website:

<http://dx.doi.org/10.1088/0004-637X/724/1/559>

Publisher's copyright statement:

Additional information:

Use policy

The full-text may be used and/or reproduced, and given to third parties in any format or medium, without prior permission or charge, for personal research or study, educational, or not-for-profit purposes provided that:

- a full bibliographic reference is made to the original source
- a [link](#) is made to the metadata record in DRO
- the full-text is not changed in any way

The full-text must not be sold in any format or medium without the formal permission of the copyright holders.

Please consult the [full DRO policy](#) for further details.

A *CHANDRA* PERSPECTIVE ON GALAXY-WIDE X-RAY BINARY EMISSION AND ITS CORRELATION WITH STAR FORMATION RATE AND STELLAR MASS: NEW RESULTS FROM LUMINOUS INFRARED GALAXIES

B. D. LEHMER^{1,2}, D. M. ALEXANDER³, F. E. BAUER^{4,5}, W. N. BRANDT^{6,7}, A. D. GOULDING³, L. P. JENKINS^{1,2}, A. PTAK²,
 AND T. P. ROBERTS³

¹ The Johns Hopkins University, Homewood Campus, Baltimore, MD 21218, USA

² NASA Goddard Space Flight Centre, Code 662, Greenbelt, MD 20771, USA

³ Department of Physics, University of Durham, South Road, Durham, DH1 3LE, UK

⁴ Pontificia Universidad Catolica de Chile, Departamento de Astronomia y Astrofisica, Casilla 306, Santiago 22, Chile

⁵ Space Science Institute, 4750 Walnut Street, Suite 205, Boulder, CO 80301, USA

⁶ Department of Astronomy & Astrophysics, 525 Davey Lab, The Pennsylvania State University, University Park, PA 16802, USA

⁷ Institute for Gravitation and the Cosmos, The Pennsylvania State University, University Park, PA 16802, USA

Received 2010 July 7; accepted 2010 September 17; published 2010 November 3

ABSTRACT

We present new *Chandra* observations that complete a sample of seventeen (17) luminous infrared galaxies (LIRGs) with $D < 60$ Mpc and low Galactic column densities of $N_{\text{H}} \lesssim 5 \times 10^{20} \text{ cm}^{-2}$. The LIRGs in our sample have total infrared (8–1000 μm) luminosities in the range of $L_{\text{IR}} \approx (1\text{--}8) \times 10^{11} L_{\odot}$. The high-resolution imaging and X-ray spectral information from our *Chandra* observations allow us to measure separately X-ray contributions from active galactic nuclei and normal galaxy processes (e.g., X-ray binaries and hot gas). We utilized total infrared plus UV luminosities to estimate star formation rates (SFRs) and *K*-band luminosities and optical colors to estimate stellar masses (M_{\star}) for the sample. Under the assumption that the galaxy-wide 2–10 keV luminosity ($L_{\text{HX}}^{\text{gal}}$) traces the combined emission from high-mass X-ray binaries (HMXBs) and low-mass X-ray binaries, and that the power output from these components is linearly correlated with SFR and M_{\star} , respectively, we constrain the relation $L_{\text{HX}}^{\text{gal}} = \alpha M_{\star} + \beta \text{SFR}$. To achieve this, we construct a *Chandra*-based data set composed of our new LIRG sample combined with additional samples of less actively star-forming normal galaxies and more powerful LIRGs and ultraluminous infrared galaxies (ULIRGs) from the literature. Using these data, we measure best-fit values of $\alpha = (9.05 \pm 0.37) \times 10^{28} \text{ erg s}^{-1} M_{\odot}^{-1}$ and $\beta = (1.62 \pm 0.22) \times 10^{39} \text{ erg s}^{-1} (M_{\odot} \text{ yr}^{-1})^{-1}$. This scaling provides a more physically meaningful estimate of $L_{\text{HX}}^{\text{gal}}$, with $\approx 0.1\text{--}0.2$ dex less scatter, than a direct linear scaling with SFR. Our results suggest that HMXBs dominate the galaxy-wide X-ray emission for galaxies with $\text{SFR}/M_{\star} \gtrsim 5.9 \times 10^{-11} \text{ yr}^{-1}$, a factor of ≈ 2.9 times lower than previous estimates. We find that several of the most powerful LIRGs and ULIRGs, with $\text{SFR}/M_{\star} \gtrsim 10^{-9} \text{ yr}^{-1}$, appear to be X-ray underluminous with respect to our best-fit relation. We argue that these galaxies are likely to contain X-ray binaries residing in compact star-forming regions that are buried under thick galactic columns large enough to attenuate emission in the 2–10 keV band ($N_{\text{H}} \gtrsim 10^{23} \text{ cm}^{-2}$).

Key words: cosmology: observations – galaxies: starburst – infrared: galaxies — X-rays: binaries — X-rays: galaxies

1. INTRODUCTION

The most energetic nearby star-forming galaxies are luminous infrared galaxies (LIRGs), which are classified as having total infrared (8–1000 μm) luminosities greater than $10^{11} L_{\odot}$ (where $L_{\odot} = 3.9 \times 10^{33} \text{ erg s}^{-1}$ is the bolometric luminosity of the Sun). The total infrared emission from most LIRGs comprises $\gtrsim 50\%$ – 90% of their galactic bolometric power output and is thought to arise primarily from dust reprocessing of obscured UV light that originates from underlying star-forming regions (see Sanders & Mirabel 1996 for a review). Therefore, the total LIRG infrared power provides an effective measure of the galactic star formation rate (SFR; e.g., Kennicutt 1998) and has been used extensively to select galaxies with active star formation (e.g., Sanders et al. 2003).

In normal star-forming galaxies (i.e., those that are not dominated by luminous active galactic nuclei (AGNs)), X-ray emission originates from X-ray binaries, supernovae, supernova remnants, hot ($\approx 0.2\text{--}1$ keV) interstellar gas, and O-stars (see, e.g., Fabbiano 1989, 2006 for reviews). Several investigations have now revealed the presence of a strong correlation between the galaxy-wide X-ray emission and total SFR (hereafter, the X-ray/SFR correlation; see, e.g., Bauer et al. 2002; Grimm

et al. 2003; Ranalli et al. 2003; Gilfanov et al. 2004a, 2004b; Persic et al. 2004; Persic & Rephaeli 2007; Lehmer et al. 2008). The X-ray/SFR correlation is thought to be driven primarily by X-ray binary emission, and at high X-ray energies (2–10 keV), where the emission intensity from hot interstellar gas and young stars decreases sharply, X-ray binaries significantly dominate the galaxy-wide X-ray power and therefore correlate strongly with SFR (e.g., Persic & Rephaeli 2002).

Detailed *Chandra* studies of nearby star-forming late-type galaxies and passive early-type galaxies have shown that the X-ray point-source emission from relatively young ($\lesssim 100$ Myr) high-mass X-ray binaries (HMXBs) and older ($\gtrsim 1$ Gyr) low-mass X-ray binaries (LMXBs) correlates well with galaxy SFR and stellar mass (M_{\star}), respectively (e.g., Grimm et al. 2003; Colbert et al. 2004; Gilfanov 2004). Colbert et al. (2004, hereafter C04) utilized *Chandra*-resolved point-source populations in 32 nearby spiral and elliptical galaxies to measure the galaxy-wide X-ray power due to point sources L_{XP} and characterize its correlation with both SFR and M_{\star} . The C04 study, which focused on representative nearby galaxies with $\text{SFR} \approx 0.01\text{--}10 M_{\odot} \text{ yr}^{-1}$ and $M_{\star} \approx 10^8\text{--}10^{11} M_{\odot}$, showed that L_{XP} is linearly correlated with both SFR and M_{\star} and the relative contributions from HMXBs and LMXBs

Table 1
LIRG Sample List and Basic Properties

Source Name (1)	<i>K_s</i> -band Source Characteristics						<i>N_H</i> (10 ²⁰ cm ⁻²) (8)	log <i>L_{IR}</i> (<i>L_⊙</i>) (9)	SFR (<i>M_⊙</i> yr ⁻¹) (10)	log <i>M_*</i> (<i>M_⊙</i>) (11)	Optical Morphology (12)	Optical Class (13)	Class Reference (14)
	α_{J2000} (hr) (2)	δ_{J2000} (deg) (3)	<i>a</i> (arcmin) (4)	<i>b</i> (arcmin) (5)	P.A. (deg) (6)	<i>D_L</i> (Mpc) (7)							
NGC 1068	02 42 41	−00 00 48	2.42	1.99	35	13.75	4.06	11.27	18.50	11.02	(R)SA(rs)b	Sy 2	1, 2, 3, 4, 5
NGC 1365	03 33 36	−36 08 25	4.60	3.45	50	18.03	1.36	11.00	9.97	11.01	SB(s)b	Sy 1	1
NGC 7552	23 16 11	−42 35 05	2.21	1.30	95	21.55	1.95	11.03	10.67	10.70	(R')SB(s)ab	H II	1, 4, 5
NGC 4418	12 26 55	−00 52 39	0.83	0.45	55	32.12	2.04	11.08	11.79	10.04	(R')SAB(s)a	LINER/Sy 2	5, 6, 7
NGC 4194	12 14 09	+54 31 37	0.64	0.44	170	40.67	1.56	11.06	11.26	10.40	IBm pec	H II	2
IC 5179	22 16 09	−36 50 37	1.48	0.56	55	47.23	1.16	11.16	14.51	10.93	SA(rs)bc	H II	2, 5
ESO 420−G013	04 13 50	−32 00 25	0.61	0.58	110	48.17	2.28	11.02	10.27	10.62	SA0 ⁺ (r) pec?	H II	4, 5
Arp 299	11 28 30	+58 34 10	1.42	1.25	28	48.24	1.05	11.88	75.60	11.05	Merger (S pec)	H II + Sy 2	6, 8, 9
NGC 838	02 09 39	−10 08 46	0.62	0.43	95	50.78	2.23	11.00	9.81	10.53	SA0 ⁰ (rs) pec?	H II	10
NGC 5135	13 25 44	−29 50 01	1.75	0.86	125	52.87	4.35	11.17	14.72	10.97	SB(s)ab	Sy 2	4, 5
NGC 5394/5	13 58 38	+37 25 28	1.53	0.80	5	54.02	1.05	11.00	9.90	11.09	SA(s)b pec	Sy 2	3
NGC 5653	14 30 10	+31 12 56	0.76	0.70	75	55.53	1.20	11.06	11.51	10.87	(R')SA(rs)b	H II	2, 5
NGC 7771	23 51 25	+20 06 43	1.52	0.62	75	57.94	4.27	11.34	21.95	11.25	SB(s)a	H II	2, 5
NGC 3221	10 22 20 ^a	+21 34 11 ^a	1.62 ^a	0.34 ^a	167 ^a	59.46	1.86	11.00	9.92	11.00	SB(s)cd? edge-on	H II	...
CGCG 049 − 057	15 13 13	+07 13 32	0.45	0.23	20	59.83	2.79	11.27	18.25	10.15	...	H II	2, 7, 5
IC 860	13 15 03	+24 37 08	0.56	0.32	20	59.88	1.12	11.17	14.51	10.36	S?	LINER/Sy2	2, 7, 5
NGC 23	00 09 53	+25 55 26	1.13	0.54	155	60.52	3.86	11.05	11.20	11.08	SB(s)a	H II	2, 5

Notes. Basic properties of our complete sample of 17 LIRGs with $D < 60$ Mpc and $N_H \lesssim 5 \times 10^{20}$ cm⁻², ordered by distance (given in Column 7). Column 1: common source name. Columns 2 and 3: right ascension and declination, respectively. Units of right ascension are hours, minutes, and seconds, and units of declination are degrees, arcminutes, and arcseconds. Column 4: semimajor axis in arcminutes. Column 5: semiminor axis in arcminutes. Column 6: position angle in degrees, measured east from north. Values given in Columns 2–6 were provided by 2MASS with the exception of NGC 3221, which was given by RC3. Column 7: luminosity distance in Mpc, as used by Sanders et al. (2003). Column 8: Galactic column density in units of 10²⁰ cm⁻² as given by Dickey & Lockman (1990). Column 9: logarithm of the total infrared (8–1000 μ m) luminosity as given by Sanders et al. (2003). Column 10: star formation rate in units of M_\odot yr⁻¹. Column 11: logarithm of the stellar mass in units of M_\odot . Columns 10 and 11 were computed following the methods presented in Section 2.2. Column 12: optical morphological classification. When available, these classifications are primarily based on RC3, with the exception of Arp 299, which was based on the Revised Shapley-Ames Catalog Of Bright Galaxies (Sandage & Tammann 1981). Column 13: optical spectroscopic classification of source type. Column 14: literature reference for Column 13; (1) Veron-Cetty & Veron 1986; (2) Veilleux et al. 1995; (3) Ho et al. 1997; (4) Kewley et al. 2001; (5) Yuan et al. 2010; (6) Armus et al. 1989; (7) Baan et al. 1998; (8) Coziol et al. 1998; (9) García-Marín et al. 2006; (10) Keel et al. 1985.

^a Values taken from RC3.

are directly dependent on the specific SFR (i.e., SFR/M_* ; a measure of the stellar-growth rate). From this perspective, the more commonly used X-ray/SFR correlation is likely to have significant scatter due to variations in M_* for a given SFR.

A recent study by Persic & Rephaeli (2007, hereafter PR07) noted that ultraluminous infrared galaxies (ULIRGs), which have $\text{SFR} \gtrsim 100 M_\odot \text{ yr}^{-1}$, have 2–10 keV luminosity-to-SFR ratios that are ~ 5 times lower than more typical nearby galaxies that have $\text{SFR} \ll 100 M_\odot \text{ yr}^{-1}$. PR07 suggest that the 2–10 keV emission in ULIRGs is likely to be dominated by HMXBs with negligible contributions from LMXBs, which likely play a more significant role in galaxies with $\text{SFR} \ll 100 M_\odot \text{ yr}^{-1}$. This trend has also been substantiated by recent *Chandra* observations of powerful LIRGs and ULIRGs from the Great Observatories All-sky LIRG Survey (GOALS; Iwasawa et al. 2009, hereafter Iw09). Despite the improved understanding of how the galaxy-wide 2–10 keV emission depends on SFR and M_* from C04 and suggestions that extremely powerful LIRGs and ULIRGs have X-ray power dominated by young HMXB populations (from, e.g., PR07; Iw09), researchers have yet to test directly and constrain the C04 relation using observations of galaxies with $\text{SFR} \gtrsim 10 M_\odot \text{ yr}^{-1}$.

In this paper, we present new *Chandra* results for a volume-limited sample ($D < 60$ Mpc) of 17 LIRGs (including 10 new LIRGs from this study; see Tables 1 and 2) with Galactic

column densities $N_H \lesssim 5 \times 10^{20}$ cm⁻² and $L_{\text{IR}} \approx 1\text{--}8 \times 10^{11} L_\odot$ ($\text{SFR} \gtrsim 10 M_\odot \text{ yr}^{-1}$; see Figures 1 and 2). We first utilize the high-resolution *Chandra* data to separate spatially and measure contributions from normal galaxy-wide X-ray emission (i.e., not due to an AGN) and AGN when present; this enables us both to investigate the X-ray/SFR correlation in detail for LIRGs and to characterize the AGN activity in the population. Using the new LIRG constraints in combination with both the *Chandra* results from C04 for less actively star-forming normal galaxies and Iw09 for more actively star-forming LIRGs and ULIRGs, we provide improved constraints upon how the normal-galaxy 2–10 keV luminosity depends on SFR and M_* , and therefore the relative contributions from HMXBs and LMXBs. This analysis has the advantage over previous studies in that it uniquely covers ~ 4 orders of magnitude in SFR and ~ 3.5 orders of magnitude in M_* and is uniformly based on *Chandra* data.

Throughout this paper, we make estimates of SFR and M_* using a Kroupa (2001) initial mass function (IMF); when making comparisons between these estimates and those quoted in other studies, we have adjusted all values to correspond to our adopted IMF. We sometimes make comparisons with the Milky Way (MW). We adopt values of $M_* \approx 5 \times 10^{10} M_\odot$ (Hammer et al. 2007), $\text{SFR} \approx 2.0 M_\odot \text{ yr}^{-1}$ (McKee & Williams 1997), and 2–10 keV luminosity $L_{\text{HX}}^{\text{gal}} = 3.3 \times 10^{39}$ erg s⁻¹ (Grimm et al. 2002) for the MW $H_0 = 70$ km s⁻¹ Mpc⁻¹, $\Omega_M = 0.3$, and $\Omega_\Lambda = 0.7$ are adopted throughout this paper (e.g., Spergel et al. 2003).

Table 2
Chandra Observation Log

Source Name	Obs. ID	Obs. Start (UT)	Exposure Time ^a (ks)	Obs. Mode ^c	Camera	Subarray? ^b (Y/N)	Pipeline Version ^d
NGC 1068	344	2000 Feb 21, 15:48	46.9	F	ACIS-S	N	7.6.11.2
	370	2000 Feb 22, 05:51	3.7	VF	ACIS-S	Y	7.6.11.1
NGC 1365	3554	2002 Dec 24, 14:57	13.6	F	ACIS-S	N	7.6.9
	6868^e	2006 Apr 17, 19:05	14.6	F	ACIS-S	Y	7.6.7.1
	6869^e	2006 Apr 20, 10:00	15.5	F	ACIS-S	Y	7.6.7.1
	6870^e	2006 Apr 23, 10:05	14.4	F	ACIS-S	Y	7.6.7.2
	6871^e	2006 Apr 10, 07:02	13.2	F	ACIS-S	Y	7.6.7.1
	6872^e	2006 Apr 12, 12:31	14.6	F	ACIS-S	Y	7.6.7.1
	6873^e	2006 Apr 14, 23:26	14.6	F	ACIS-S	Y	7.6.7.1
NGC 7552	7848	2007 Mar 31, 05:48	5.1	F	ACIS-S	N	7.6.11
NGC 4418	4060	2003 Mar 10, 00:58	19.8	F	ACIS-S	Y	7.6.8
	10391	2009 Feb 20, 20:34	5.7	VF	ACIS-S	Y	7.6.11.10
NGC 4194	7071	2006 Sep 9, 23:30	35.0	F	ACIS-S	N	7.6.8.1
IC 5179	10392	2009 Jun 21, 13:51	12.0	VF	ACIS-S	Y	7.6.11.10
ESO 420–G013	10393	2009 May 13, 05:46	12.4	VF	ACIS-S	Y	7.6.11.10
Arp 299	1641	2001 Jul 13, 11:07	24.3	F	ACIS-I	Y	7.6.9
NGC 838	10394	2008 Nov 23, 09:03	13.8	VF	ACIS-S	Y	7.6.11.9
NGC 5135	2187	2001 Sep 4, 15:23	26.4	F	ACIS-S	Y	7.6.9
NGC 5394/5	10395	2009 Mar 18, 23:28	15.7	VF	ACIS-S	Y	7.6.11.10
NGC 5653	10396	2009 Apr 11, 05:46	16.5	VF	ACIS-S	Y	7.6.11.10
NGC 7771	10397	2009 May 22, 05:12	16.7	VF	ACIS-S	Y	7.6.11.10
NGC 3221	10398	2009 Mar 19, 04:19	19.0	VF	ACIS-S	Y	7.6.11.10
CGCG 049 – 057	10399	2009 Apr 17, 05:43	19.1	VF	ACIS-S	Y	7.6.11.10
IC 860	10400	2009 Mar 24, 02:38	19.1	VF	ACIS-S	Y	7.6.11.10
NGC 23	10401	2008 Oct 27, 06:22	19.4	VF	ACIS-S	Y	7.6.11.9

Notes. Links to the data sets in this table have been provided in the electronic edition.

^a All observations were continuous. These times have been corrected for removed data that was affected by high background, see Section 3.

^b States whether a subarray was used in the observation.

^c The observing mode (F: faint mode; VF: very faint mode).

^d The version of the CXC pipeline software used for basic processing of the data.

^e Observation covers only a small fraction of the galactic extent and was therefore not used in the analyses presented in this paper.

2. SAMPLE

2.1. LIRG Sample Selection

Using the *IRAS* Revised Bright Galaxies Sample (RBGS; Sanders et al. 2003), we constructed a sample of nearby LIRGs that were at distances less than 60 Mpc and had Galactic column densities $N_{\text{H}} < 5 \times 10^{20} \text{ cm}^{-2}$ (Dickey & Lockman 1990). The former requirement results in *Chandra* imaging resolution of $\lesssim 150$ pc in the region of the nucleus, which allows for reasonable distinction between nuclear AGNs and starburst regions (see, e.g., Levenson et al. 2004 for an analysis of the AGN plus starburst nucleus of NGC 5135 in our sample). The latter requirement results in moderate-to-good Galactic transparency to soft X-ray emission, which is valuable for detecting and modeling the emission from hot ≈ 0.5 –1 keV gas that is often found in star-forming galaxies. In total, 36 RBGS LIRGs reside at $D < 60$ Mpc and 17 satisfy our Galactic column density criterion. In Table 1, we provide the basic properties of our LIRG sample, and in Figure 1, we show Digitized Sky Survey (DSS) red images of the galaxies in our sample. In contrast to ULIRGs, which are nearly all late-type galaxies with evidence for mergers/interactions (e.g., Melnick & Mirabel 1990; Sanders et al. 1988; Chen et al. 2010), the LIRGs that make up our sample consist of a variety of optical morphological types (e.g., spirals, barred spirals, S0s) with only a small fraction ($\sim 10\%$) showing evidence for mergers/interactions.

In Figure 2, we show the infrared luminosity L_{IR} versus distance for the RBGS and highlight our sample (filled black circles). Of the 17 LIRGs in our sample, 7 (NGC 1068, NGC 1365, NGC 7552, NGC 4418, NGC 4194, Arp 299, and NGC 5135) had *Chandra* archival data. Detailed *Chandra* analyses for these sources can be found in the literature for NGC 1068 (Young et al. 2001; Smith & Wilson 2003), NGC 1365 (Risaliti et al. 2009a, 2009b; Soria et al. 2009; Strateva & Komossa 2009; Wang et al. 2009), NGC 4194 (Kaaret & Alonso-Herrero 2008), Arp 299 (Zezas et al. 2003), and NGC 5135 (Levenson et al. 2004). To enable new *Chandra* constraints on the LIRG population in general, we proposed successfully in *Chandra* Cycle 10 (PI: D. M. Alexander) to observe the remaining 10 LIRGs. Our *Chandra* program (and consequently adopted exposure times; see Table 2) was designed to allow for the detection of ultraluminous X-ray sources (ULXs) down to a 0.5–8 keV limit of $\approx 2 \times 10^{39} \text{ erg s}^{-1}$ for the 17 LIRGs. In a forthcoming paper (F. E. Jackson et al. 2011, in preparation), we will present the X-ray and statistical properties of the ULX populations detected in the LIRG sample.

As is evident from Figure 2, our sample provides a useful complement to the L_{IR} distribution of *Chandra*-observed galaxies between less active nearby galaxies (e.g., from C04) and more powerful LIRGs and ULIRGs (e.g., from the GOALS; Iw09). We note that the RBGS sources with *Chandra* observations highlighted in Figure 2 do *not* constitute a complete census of the *Chandra* archive. However, incompleteness is only

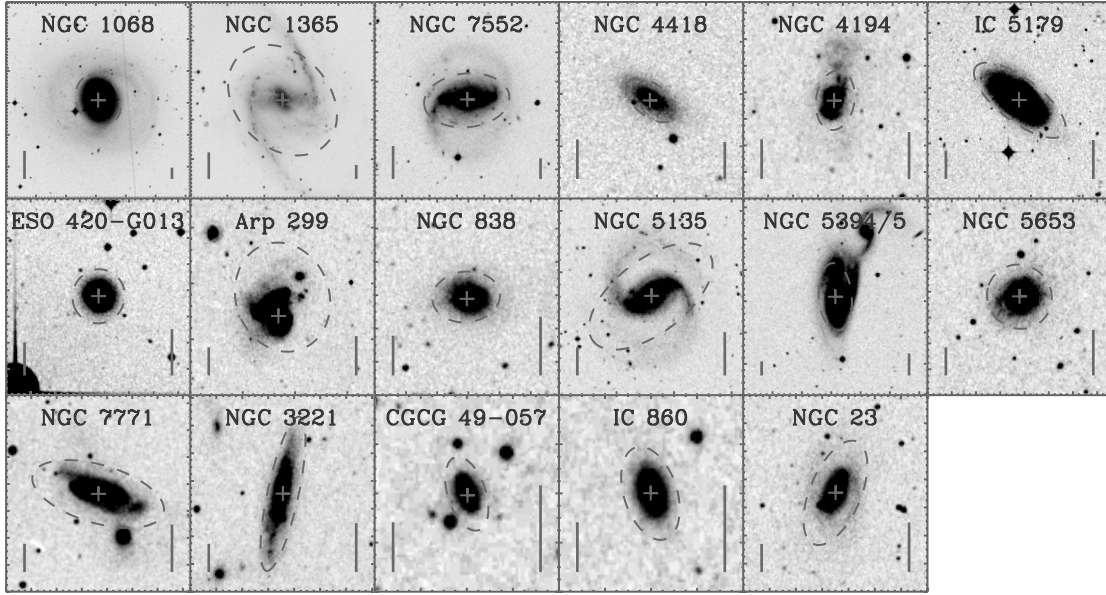


Figure 1. Digitized Sky Survey (DSS) red images of each of the 17 LIRGs that make up our sample. The panel sizes presented here vary to illustrate galaxy morphology most clearly, and in the lower left and right corners of each panel, we have provided vertical reference bars with physical sizes of 10 kpc and angular sizes of 1 arcmin, respectively. Dashed gray ellipses represent the total K_s -band galaxy size and orientation as described in Columns 2–6 of Table 1 and gray crosses indicate the adopted locations for the galactic nuclei (see Section 4.2 for details). These images show that the galaxies making up our LIRG sample have a diversity of optical morphological types, physical sizes, and inclinations.

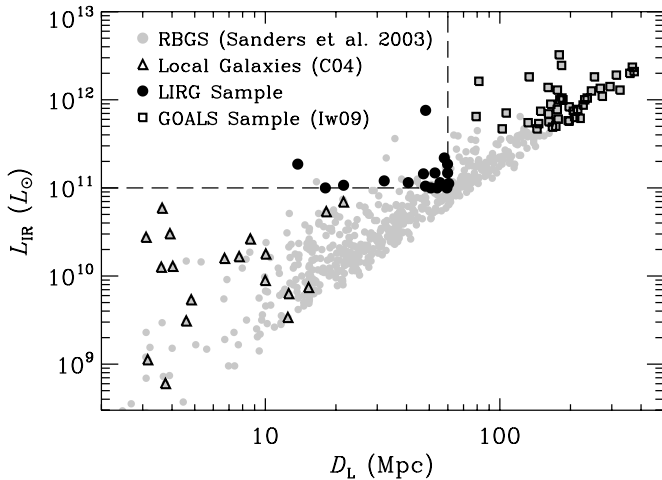


Figure 2. Total infrared (8–1000 μm) luminosity L_{IR} vs. distance for IRAS sources (light-gray filled circles), as provided by Sanders et al. (2003). Our complete sample of *Chandra*-observed LIRGs that have $D < 60$ Mpc and $N_{\text{H}} \lesssim 5 \times 10^{10} \text{ cm}^{-2}$ (dashed boundary lines) are indicated with black filled circles. Nearby normal late-type galaxies that have been studied extensively with *Chandra* have been highlighted with open triangles (C04) and LIRGs/ULIRGs from the Great Observatories All-sky LIRG Survey (GOALS) sample (Iw09) are indicated with open squares. Our sample provides new constraints in the range between nearby normal galaxies and powerful LIRGs/ULIRGs.

most severe for galaxies with $L_{\text{IR}} \lesssim 10^{11} L_{\odot}$, which are not the primary focus of this analysis; detailed *Chandra* and multiwavelength studies of such galaxies will be the subject of forthcoming work by the *Spitzer* Infrared Nearby Galaxies Survey (SINGS) collaboration (L. P. Jenkins et al. 2011, in preparation; A. Ptak et al. 2011, in preparation; see Kennicutt et al. 2003 for survey details). For LIRGs and ULIRGs, the *Chandra* observations highlighted in Figure 2 are nearly complete.

2.2. Stellar Mass and Star Formation Rate Estimates

We estimated stellar masses for the LIRGs in our sample following the prescription outlined in Appendix 2 of Bell

et al. (2003), which provides galaxy mass-to-light ratios in several optical/near-IR bands as a function of optical/near-IR color. We utilized $B - V$ colors from the NASA/IPAC Extragalactic Database (NED), which were primarily from the Third Reference Catalog of Bright Galaxies (RC3; de Vaucouleurs et al. 1991). K -band luminosities were computed using data from the Two Micron All Sky Survey (2MASS) large galaxy atlas (Jarrett et al. 2003) and K_s -band extended source catalogs.⁸ We note that for NGC 3221, no 2MASS counterpart was available, and we therefore adopted the M_{\star} estimate provided by the GOALS team (Howell et al. 2010, hereafter H10), adjusted to match our adopted distance and IMF (see below). For the 16 LIRGs having 2MASS counterparts, we computed stellar masses using the following equation:

$$\log M_{\star}/M_{\odot} = \log L_K/L_{K,\odot} + 0.135(B - V) - 0.356. \quad (1)$$

The numerical constants in Equation (1) were supplied by Table 7 of Bell et al. (2003) and are appropriate for our choice of $B - V$ color and L_K ; the normalization has been adjusted by 0.15 dex to account for our adopted Kroupa (2001) IMF. Uncertainties at the ≈ 0.1 dex level are expected due to variations in stellar ages, dust attenuation, and bursts of star formation (see Bell et al. 2003 for further details).

We note that 12 of the LIRGs in our sample (including 11 LIRGs with stellar mass estimates from Equation (1)) have been studied extensively from the far-UV to IR (including observations with both *Galaxy Evolution Explorer* (GALEX) and *Spitzer*) by the GOALS collaboration and have stellar mass estimates available (e.g., Armus et al. 2009; H10). After accounting for known differences in adopted distances and IMF, we find that our stellar mass estimates are in good agreement with those of H10, with our values being larger by $\approx 4\%$ (median value) with a 1σ scatter of ≈ 0.09 dex.

⁸ The 2MASS extended source catalog is available online via <http://tdc-www.harvard.edu/catalogs/tmxsc.html>

By selection, our LIRG sample consists of galaxies radiating powerfully over the far-IR (8–1000 μm) wavelength range. The far-IR light is expected to be produced by dust-reprocessed emission from underlying UV-obscured star formation activity and can therefore be used as a direct measurement of the SFR. Using the 8–1000 μm total infrared luminosities L_{IR} provided by Sanders et al. (2003) and the methods described in Section 3.2 of Bell et al. (2005), we estimated the total galaxy SFR using the following equation:

$$\text{SFR}(M_{\odot} \text{ yr}^{-1}) = \gamma 9.8 \times 10^{-11} L_{\text{IR}}, \quad (2)$$

where L_{IR} is expressed in units of solar bolometric luminosity ($L_{\odot} = 3.9 \times 10^{33} \text{ erg s}^{-1}$) and the factor $\gamma = 1.000\text{--}1.024$ provides small corrections that account for UV emission emerging from unobscured star-forming regions. Equation (2) is a direct variant of Equation (1) presented by Bell et al. (2005) and was derived from PEGASE stellar-population models, which assumed a 100 Myr old population with constant SFR and a Kroupa (2001) IMF. This calibration uses identical assumptions to the SFR calibrations provided by Kennicutt (1998). For the 12 LIRGs that overlap with the H10 sample, γ was provided by H10 using values of the total infrared flux from *IRAS* (f_{IR}) and the far-UV flux (f_{FUV}) from *GALEX*: $\gamma \equiv 1 + f_{\text{FUV}}/f_{\text{IR}}$. For these 12 LIRGs, we find good agreement between SFR measurements, with our SFR values being larger by $\approx 4\%$ (median offset) with small scatter ($\approx 0.003 \text{ dex}$; 1σ). For the five LIRGs in our sample without H10 counterparts, we adopted $\gamma^{\text{median}} \approx 1.017$, the median value of γ for the 12 LIRGs with H10 counterparts.

In Table 1, we provide the derived stellar masses and SFRs for our LIRGs. The sample spans $M_{\star} \approx (1.3\text{--}16) \times 10^{10} M_{\odot}$ (median value of $M_{\star} \approx 7.2 \times 10^{10} M_{\odot}$) and $\text{SFR} = 9.8\text{--}75.6 M_{\odot} \text{ yr}^{-1}$ (median value of $\text{SFR} \approx 11 M_{\odot} \text{ yr}^{-1}$). For comparison, the LIRGs/ULIRGs from the *Chandra* GOALS project (Iw09) span a similar range of stellar masses ($M_{\star} \approx (1.6\text{--}27) \times 10^{10} M_{\odot}$; median value of $M_{\star} \approx 6.5 \times 10^{10} M_{\odot}$), but contain more actively star-forming galaxies ($\text{SFR} \approx 14\text{--}215 M_{\odot} \text{ yr}^{-1}$; median value of $\text{SFR} \approx 68 M_{\odot} \text{ yr}^{-1}$). The nearby late-type galaxies in the C04 study span the stellar mass range of $\approx 6 \times 10^7\text{--}10^{11} M_{\odot}$ (median value of $M_{\star} \approx 1.8 \times 10^{10} M_{\odot}$) and less powerful star-forming galaxies with $\text{SFR} = 0.03\text{--}5.6 M_{\odot} \text{ yr}^{-1}$ (median value of $\text{SFR} = 0.8 M_{\odot} \text{ yr}^{-1}$).

3. CHANDRA OBSERVATIONS AND DATA REDUCTION

In Table 2, we present the *Chandra* ACIS observation log for our LIRG sample. Our analyses began with the *Chandra* X-ray Center (CXC) processed Level 2 events files, which were all processed using pipeline version 7.6.8 or greater. Additional reductions and analysis of the data were performed using the *Chandra* Interactive Analysis of Observations (CIAO) version 4.1 tools and custom software. We screened our events files for undesirable grades using the standard ASCA grade set (ASCA grades 0, 2, 3, 4, 6) and excluded from the events lists background flaring events that were $\geq 3\sigma$ times higher than normal. For observations 344 (NGC 1068), 3554 (NGC 1365), 7071 (NGC 4194), and 2187 (NGC 5135), we removed short flaring events lasting ≈ 0.5 , 1.0, 0.5, and 3.0 ks, respectively.

Out of the 17 LIRGs in our sample, three galaxies (NGC 1068, 1365, and 4418) have more than one *Chandra* observation available. However, in the case of NGC 1365, observations 6868, 6869, 6870, 6871, 6872, and 6873 cover only a small

fraction of the entire galactic extent as defined in Table 1 and constitute $\approx 86.5\%$ of the total ACIS exposure available. In order to avoid galaxy-wide spectral fits (see Section 4.1) that are statistically biased toward these smaller non-representative regions, we therefore chose for this study to make use of only observation 3554, which covers the entire galactic extent and is sufficiently sensitive for our study.

For the remaining two LIRGs with more than one *Chandra* observation (NGC 1068 and 4418), we corrected the relative astrometry to match the frames with the longest exposures. We first ran *wavdetect* at a false-positive probability threshold of 10^{-6} to create point-source catalogs for each frame. For a given galaxy, we filtered each of our *wavdetect* catalogs to include only sources that were common to all frames and within $6'$ of the *Chandra* aim point, where the point-spread function size and resulting positional errors are small. Using these source lists, we registered each aspect solution and events list to the frame with the longest exposure time using the CIAO tools *reproject_aspect* and *reproject_events*, respectively. The resulting astrometric reprojections gave nearly negligible linear translations (< 0.38 pixels), rotations (< 0.1 deg), and stretches ($< 0.06\%$ of the pixel size). Using the astrometrically reprojected events lists, we combined the observations using *dmmerge* to create merged events lists.

Using the events lists, we constructed images of each LIRG in three bands: 0.5–8 keV (full band; FB), 0.5–2 keV (soft band; SB), and 2–8 keV (hard band; HB). For each of the three bands, we constructed corresponding exposure maps following the basic procedure outlined in Section 3.2 of Hornschemeier et al. (2001); these maps were normalized to the effective exposures of sources located at the aim points. This procedure takes into account the effects of vignetting, gaps between the CCDs, bad column and pixel filtering, the spatially dependent degradation of the ACIS optical blocking filter, and the reduced area of frames that use subarrays (see Table 2). A photon index of $\Gamma = 1.4$, the slope of the extragalactic cosmic X-ray background in the FB (e.g., Hickox & Markevitch 2006), was assumed in creating the exposure maps.

4. ANALYSES

4.1. Extraction of Total LIRG X-ray Properties

To measure the total galaxy-wide X-ray emission originating from each of the LIRGs, we began by extracting *total galactic counts* $S_{\text{tot}}^{\text{gal}}$ and effective exposure times $T_{\text{tot}}^{\text{gal}}$ from each of the three images and exposure maps using elliptical regions that approximate the galactic stellar extent. Whenever possible, we adopted for these elliptical regions the “total” semimajor/minor axes and position angles provided by the 2MASS large galaxy atlas (Jarrett et al. 2003) and the K_s -band extended source catalogs; these regions, which were determined using a curve-of-growth analysis (see Section 4.2 of Jarrett et al. 2003), are shown in Figure 1 (dashed ellipses) and their values are tabulated in Table 1. For NGC 3221, 2MASS values were not available and we therefore adopted the RC3 values for the semimajor/minor axes and position angle for this galaxy. We note that for 14 of the 17 LIRGs in our sample, both 2MASS and RC3 galaxy extent parameters were available. We find that the 2MASS values of major and minor axes are on average larger than those of RC3 by only small factors of ≈ 1.13 and ≈ 1.08 , respectively.

To estimate the background contributions to the total counts for each galaxy, we extracted *background counts* $S_{\text{bkg}}^{\text{gal}}$ and

Table 3
Basic X-ray Properties and Spectral Fitting Results

Source Name (1)	Net Counts		Γ (4)	kT (keV) (5)	χ^2/ν (6)	ν (7)	$\log L_{\text{HX}}^{\text{gal}}$ (erg s ⁻¹) (8)	$\Phi_{2-8\text{keV}}^{\text{nuc}}/\Phi_{2-8\text{keV}}^{\text{gal}}$ (9)	Other Evidence for AGN (10)	AGN Dominant? (Y/N) (11)
	(0.5–8 keV) (2)	(2–8 keV) (3)								
NGC 1068	150875 ± 404	11215 ± 131	41.49 ^a	0.74 ^a	Opt., IR, X-ray	Y
NGC 1365	4719 ± 127	841 ± 90	1.88 ± 0.12	0.73 ± 0.05	1.26	84	40.65	0.88	Opt., IR, X-ray	Y
NGC 7552	939 ± 40	113 ± 23	2.06 ± 0.13	0.64 ± 0.04	0.91	46	40.40	<0.08	...	N
NGC 4418	49 ± 23	<53	3.28 ± 0.46	<39.58	N
NGC 4194	2413 ± 53	263 ± 24	2.11 ± 0.08	0.83 ± 0.02	1.23	79	40.43	0.50	IR	Y
IC 5179	520 ± 33	62 ± 22	2.10 ± 0.19	0.84 ± 0.06	0.62	32	40.49	<0.09	...	N
ESO 420–G013	762 ± 31	53 ± 15	3.00 ± 0.19	0.71 ± 1.61	1.09	30	40.08	0.43	Opt., IR	N
Arp 299	4456 ± 72	836 ± 36	1.85 ± 0.06	0.80 ± 0.02	1.29	130	41.32	0.11	Opt., IR, X-ray	N
NGC 838	632 ± 29	70 ± 14	2.07 ± 0.13	0.73 ± 2.84	0.83	28	40.61	0.41	...	N
NGC 5135	3756 ± 74	346 ± 37	2.53 ± 0.08	0.78 ± 0.55	1.35	117	40.70	0.44	Opt., IR, X-ray	N
NGC 5394/5	289 ± 38	92 ± 30	1.69 ± 0.38	0.09 ± 0.20	0.65	37	40.49	0.27	Opt.	N
NGC 5653	389 ± 30	50 ± 19	2.21 ± 0.26	0.68 ± 0.06	1.20	26	40.18	<0.11	...	N
NGC 7771	864 ± 42	233 ± 30	1.24 ± 0.21	0.63 ± 2.39	1.03	55	41.18	0.53	IR, X-ray	Y
NGC 3221	310 ± 31	69 ± 22	1.58 ± 0.16	≈0.0 ^b	0.95	26	40.66	0.40	...	N
CGCG 049 – 057	33 ± 13	<29	1.05 ± 0.57	<40.29	N
IC 860	<44	<35	≈2.0 ^c	<40.19	N
NGC 23	717 ± 38	<71	2.03 ± 0.21	0.73 ± 1.12	1.18	41	<40.54	>0.24	...	N

Notes. Basic X-ray properties and spectral fitting results for the LIRGs in our sample. Column 1: source name. Columns 2 and 3: net source counts in the 0.5–8 keV and 2–8 keV bandpasses, respectively (see Section 4.1 for details). For sources with ≥ 300 FB counts listed in Column 2, X-ray spectral fitting was performed over the 0.5–8 keV band. Columns 4 and 5: best-fit values of Γ and kT , respectively, for an assumed power-law plus Raymond–Smith thermal plasma model (see Section 4.1 for details). Columns 6 and 7: reduced χ^2 value (χ^2/ν) and the number of degrees of freedom in the fits (ν), respectively. Column 8: integrated 2–10 keV total luminosity, computed using our best-fit models and distances provided in Table 1, Column 7. Column 9: ratio of 2–8 keV count rates from the nuclear region of each galaxy and the total galaxy-wide extent. Count rates were computed following the methods described in Sections 4.1 and 4.2. A source with large nuclear contributions to the total 2–8 keV count rates harbors either an AGN or a strong nuclear starburst. Column 10: notes whether there is evidence for AGN activity via optical spectroscopy (“Opt.”; see Columns 13 and 14 in Table 1), the mid-infrared spectrum (“IR”), or from X-ray studies in the literature (“X-ray”); see Section 4.2. Column 11: indicates whether the integrated 2–10 keV luminosity (Column 8) is dominated by AGN activity. We consider sources that have both $\Phi_{2-8\text{keV}}^{\text{nuc}}/\Phi_{2-8\text{keV}}^{\text{gal}} \geq 0.5$ (Column 9) and additional evidence for AGN activity from Column 10 to have the 2–10 keV luminosity dominated by an AGN (“Y”); otherwise, we consider the galaxy to be dominated by X-ray binary emission (“N”).

^a Values are inferred using detailed analysis by Young et al. (2001).

^b Best-fit spectrum did not require the use of a hot gas component.

^c A simple power-law model with $\Gamma \approx 2.0$ was assumed for IC 860.

exposure times $T_{\text{bkg}}^{\text{gal}}$ for each of the three images using 3–5 moderate size (≈ 20 –90 arcsec radius) circular regions that were outside the galactic K_s -band ellipses and did not overlap within 10'' of the galaxy or any sources detected by wavdetect at a false-positive probability threshold of 10^{-6} .

Using the galaxy and background counts, we estimated the net galaxy-wide LIRG counts $N^{\text{gal}} = S_{\text{tot}}^{\text{gal}} - S_{\text{bkg}}^{\text{gal}} T_{\text{tot}}^{\text{gal}}/T_{\text{bkg}}^{\text{gal}}$ for each of the three bands. Since $T_{\text{tot}}^{\text{gal}}$ and $T_{\text{bkg}}^{\text{gal}}$ are computed using the sum of exposure map values over the source and background regions, respectively, the estimated background contribution to the net counts (i.e., $S_{\text{bkg}}^{\text{gal}} T_{\text{tot}}^{\text{gal}}/T_{\text{bkg}}^{\text{gal}}$) are corrected for both extraction area and vignetting. We note that while these background estimates will account for emission due to unrelated background X-ray sources (e.g., distant AGNs; see, e.g., Moretti et al. 2003; Bauer et al. 2004; Kim et al. 2007) that fall below our source detection threshold, these estimates do not include contributions from unrelated sources that are detected in the X-ray band that may lie within the extent of the galaxy. Using the best-fit $\log N$ – $\log S$ from Moretti et al. (2003) and the elliptical galaxy areas described in Columns 2–6 of Table 1, we estimate that unrelated X-ray detected sources are expected to contribute $\lesssim 8\%$ (median $\approx 2\%$) to the total 2–8 keV band count rate of each LIRG in our sample. Since these contributions are small and subject to large uncertainties, we therefore

do not make any additional corrections to the net galaxy count rates.

We considered a source to be *detected* in a given band if the signal-to-noise ratio ($S/N = N^{\text{gal}}/[S_{\text{bkg}}^{\text{gal}} T_{\text{tot}}^{\text{gal}}/T_{\text{bkg}}^{\text{gal}}]^{0.5}$) was greater than or equal to three. When a source was not detected in a given band, we computed 3σ upper limits on its net counts. In Columns 2 and 3 of Table 3, we provide the net 0.5–8 keV and 2–8 keV source counts for the 17 LIRGs in our sample, and in Figure 3, we show their 0.5–8 keV adaptively smoothed images. We note that all galaxies, with the exception of IC 860, are detected in the FB. In the HB, NGC 4418, CGCG 049–057, IC 860, and NGC 23 are undetected. The LIRGs have net FB source counts in the range of ≈ 30 – 10^5 counts; for the 16 sources that were detected in the FB, X-ray spectral fitting was performed.

To model the basic spectral properties of the FB detected LIRGs in our sample, we utilized the X-ray spectral modeling program xspec version 12.5.1 (Arnaud 1996). We note that the galaxy-wide and nuclear spectral properties of the LIRG NGC 1068 have been studied extensively in the literature by, e.g., Young et al. (2001); hereafter, we adopt the complex best-fit spectral models and resulting properties provided by Young et al. (2001).

For each observation of the remaining 15 galaxies with FB detections, we employed the CIAO tool specextract to

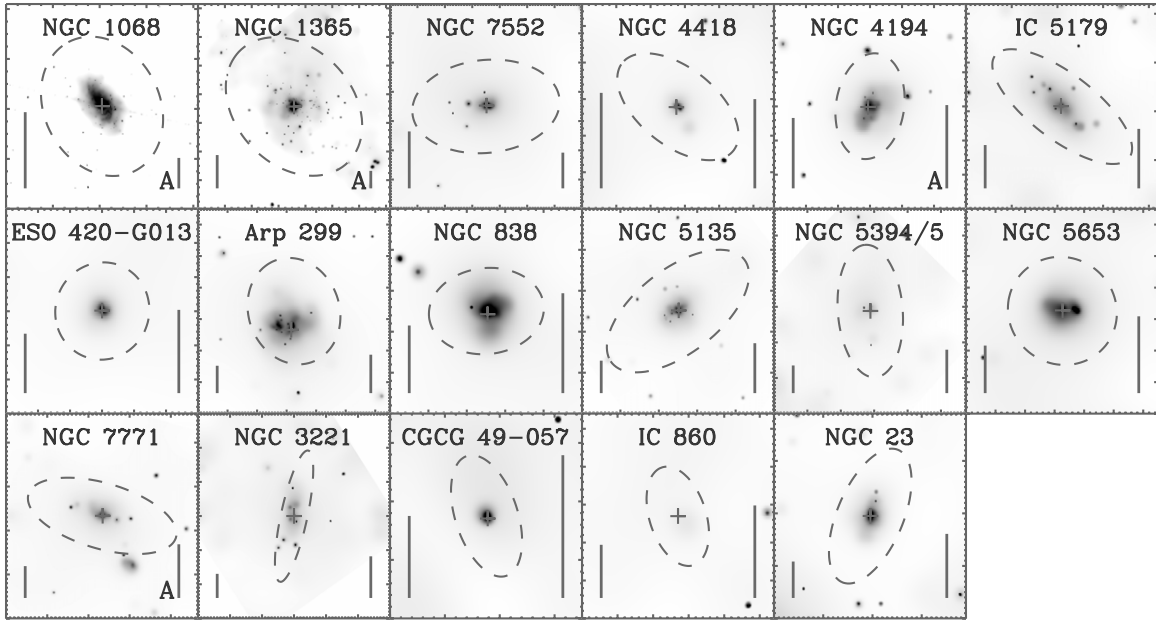


Figure 3. Full band (0.5–8 keV) adaptively smoothed images of the 17 LIRGs in our sample. The images were created using the CIAO tool `csmooth`, applied to the raw images at the 2.5σ level. Symbols and scales have the same meaning as they did in Figure 1; however, the image sizes have been adjusted to show most clearly the X-ray morphologies of the galaxies. Galaxies with 2–8 keV emission dominated by an AGN component (see Section 4.2) have been denoted with an “A” in the lower right. We note that each image has a different exposure time (see Table 2) and the smoothed-image sharpness generally increases with increasing exposure time.

construct source and background spectra, response matrix files (RMFs), and properly weighted ancillary response files (ARFs) over the source and background regions described above. For the 13 FB detected LIRGs that had $\gtrsim 300$ net counts (excluding NGC 1068), we utilized χ^2 fitting of the data grouped in bins with a minimum of 20 counts. For these galaxies, we assumed a simple spectral model consisting of Galactic absorption (as given in Column 8 of Table 1), a Raymond–Smith thermal plasma (from hot gas associated with star formation activity) with solar abundances, plus a power-law component (originating from X-ray binaries and AGN when present). Similar composite fits have been performed successfully for ULIRGs (see, e.g., Franceschini et al. 2003; Ptak et al. 2003). We find that our simple model provides a reasonable fit to these 13 LIRGs ($\chi^2/\nu = 0.62$ – 1.35 ; median $[\chi^2/\nu] = 1.09$). For NGC 3221, we find that the best-fit plasma component provides only a negligible contribution to the total spectrum; we therefore fit the X-ray spectrum using only a power-law model. For the remaining two FB detected LIRGs that had ≈ 30 – 50 net counts (NGC 4418 and CGCG 049–057), we performed simple power-law fits to the unbinned spectral data by minimizing the Cash statistic (Cash 1979). For NGC 4418, which was observed in two exposures (see Table 2), we performed joint-spectral fitting of the two observations.

The galaxy-wide best-fit model parameters are provided in Table 3. Using these models and the distances provided in Column 7 of Table 1, we computed the total galaxy-wide 2–10 keV power output $L_{\text{HX}}^{\text{gal}}$. For sources that were not detected in the HB, we computed 3σ upper limits to $L_{\text{HX}}^{\text{gal}}$ using our best-fit spectral model renormalized to the 3σ upper limit on the 2–8 keV count rate. In the case of IC 860, which was not detected in the FBs or HBs, we assumed a simple power-law model with $\Gamma = 2.0$. Our best estimate values of $L_{\text{X}}^{\text{gal}}$ are provided in Column 8 of Table 3. Using our spectral fits, we estimate that hot gas emission will provide only a negligible contribution ($< 6.5\%$ for all LIRGs) to the total 2–10 keV emission for our LIRGs. We

therefore expect that LIRGs that do not harbor a luminous AGN (see Section 4.2) will have $L_{\text{HX}}^{\text{gal}}$ dominated by X-ray binary emission.

4.2. AGN Contribution to Total Galaxy X-ray Emission

As noted in Columns 13 and 14 of Table 1, ≈ 5 – 7 of the LIRGs in our sample have been identified to harbor an AGN via optical spectroscopy. Additional evidence for AGN activity in these LIRGs has been observed in *Spitzer* infrared spectrograph (IRS) data available from the archive for the entire sample. These data were analyzed following the methods outlined in Goulding & Alexander (2009). The *Spitzer* data reveal emission-line features (e.g., [Ne V] $\lambda 14.3 \mu\text{m}$ or $24.3 \mu\text{m}$) indicative of AGN activity for NGC 1068, NGC 1365, NGC 4194, ESO 420–G013, NGC 5135, and NGC 7771, and in the case of Arp 299 a hot-dust component from an AGN has been identified by Alonso-Herrero et al. (2009). Furthermore, X-ray studies of NGC 1068 (e.g., Ogle et al. 2003), NGC 1365 (e.g., Risaliti et al. 2009b), Arp 299 (e.g., Della Ceca et al. 2002), NGC 5135 (Levenson et al. 2004), and NGC 7771 (Jenkins et al. 2005) have revealed X-ray spectral signatures of AGN activity (primarily through the presence of a heavily absorbed X-ray emission component and/or Fe K emission lines). In Column 10 of Table 3, we highlight whether a source has evidence for AGN activity from the optical, infrared, and/or X-ray bands.

In cases where the AGN is luminous in the X-ray band, the AGN component will dominate the integrated (galaxy-wide plus nuclear) 2–10 keV power $L_{\text{HX}}^{\text{gal}}$ (Column 8 of Table 3). In a forthcoming paper (P. S. Stratford et al. 2011, in preparation), we will present multiwavelength analyses that characterize the detailed accretion properties of the AGNs in our LIRG sample; however, for our purposes, we are primarily interested in how the galaxy-wide 2–10 keV emission from X-ray binaries correlates with SFR and M_* and therefore remove the sources that have 2–10 keV emission dominated by AGN activity.

To estimate the AGN contribution to $L_{\text{HX}}^{\text{gal}}$ for each LIRG, we began by estimating the position of the nucleus of each galaxy. For the majority of the LIRGs, the nucleus was isolated first by eye using the DSS red images and then by choosing manually the wavdetect position of the brightest 0.5–8 keV source within the optical nuclear region. The adopted LIRG nuclei are generally consistent with the apparent optical nuclei; their locations are shown in Figures 1 and 3 (gray crosses). In most cases, the X-ray nucleus can be obviously characterized as a bright point source at the center of diffuse X-ray emission or a single point source at the center of the optical nuclear region. However, for Arp 299 and NGC 5135, there was more than one possible choice for the central nuclear X-ray source; for these galaxies, we adopted the positions of the AGN components noted by Zezas et al. (2003) and Levenson et al. (2004), respectively. Furthermore, for NGC 5653 and IC 860, there were no obvious central X-ray point sources to identify as the nucleus; we therefore estimated by eye the nuclear positions of these galaxies using the DSS red images.

At the nuclear position of each source, we extracted nuclear source counts $S_{\text{tot}}^{\text{nuc}}$ and mean exposure times $T_{\text{tot}}^{\text{nuc}}$ from the 2–8 keV images and exposure maps, respectively, using a circular aperture with radius equal to the $\approx 90\%$ encircled-energy fraction radius (Feigelson et al. 2000).⁹ We estimated the local nuclear background count rate for each source by extracting nuclear background counts $S_{\text{bkg}}^{\text{nuc}}$ and exposure times $T_{\text{bkg}}^{\text{nuc}}$ from an annulus centered on the nuclear position with inner and outer radii equal to 1.5 and 2.5 times the $\approx 90\%$ encircled-energy fraction radius, respectively. The net nuclear 2–8 keV count rates $\Phi_{2-8\text{keV}}^{\text{nuc}} = S_{\text{tot}}^{\text{nuc}}/T_{\text{tot}}^{\text{nuc}} - S_{\text{bkg}}^{\text{nuc}}/T_{\text{bkg}}^{\text{nuc}}$ were then computed and compared with the total galaxy-wide count rates $\Phi_{2-8\text{keV}}^{\text{gal}}$ computed in Section 4.1.

In Column 9 of Table 3, we provide $\Phi_{2-8\text{keV}}^{\text{nuc}}/\Phi_{2-8\text{keV}}^{\text{gal}}$ for the LIRGs in our sample. We note that for NGC 1068, we utilized the nuclear and galaxy-wide 2–10 keV luminosities provided by Young et al. (2001). Sources without listed values of $\Phi_{2-8\text{keV}}^{\text{nuc}}/\Phi_{2-8\text{keV}}^{\text{gal}}$ had both galactic and nuclear components that were undetected in the 2–8 keV band. For NGC 23, the nucleus was detected in the 2–8 keV band, but due to the increased background over the larger galaxy-wide area, the total galaxy emission was formally undetected; for this source, we listed the 3σ lower limit on $\Phi_{2-8\text{keV}}^{\text{nuc}}/\Phi_{2-8\text{keV}}^{\text{gal}}$. We consider the observed 2–10 keV emission of the LIRGs to be “AGN dominant” if there is both evidence for AGN activity from the optical, infrared, and/or X-ray as noted in Column 10 in Table 3 and $\Phi_{2-8\text{keV}}^{\text{nuc}}/\Phi_{2-8\text{keV}}^{\text{gal}} \geq 0.5$ (see Column 9 of Table 3). We find that NGC 1068, NGC 1365, NGC 4194, and NGC 7771 satisfy these conditions. In Sections 5 and 6, we study galaxies with 2–10 keV emission dominated by X-ray binary populations, and therefore exclude the four AGN-dominant LIRGs from our further analyses. We note that a few of the remaining “normal” LIRGs in our sample harbor AGNs, which likely provide some contribution to the nuclear 2–10 keV emission. However, since we generally expect that the unresolved nucleus (at scales $\lesssim 500$ pc) will also contain powerful star formation regions (e.g., Scoville et al. 2000; Alonso-Herrero et al. 2006a), which will contribute to the total galaxy-wide X-ray binary emission, we do not attempt to subtract any AGN component in estimating $L_{\text{HX}}^{\text{gal}}$.

5. RESULTS

In this section, we explore the correlation between X-ray luminosity and SFR using exclusively *Chandra* data from the nearby normal galaxies from C04, LIRGs from this work, and LIRGs/ULIRGs from GOALS (Iw09); hereafter, we refer to these three data sets collectively as the *full Chandra sample*. In the analyses that follow, we have removed galaxies that are observed to harbor an X-ray luminous AGN, and for the C04 sample, we removed early-type galaxies that do not have accurate measures of SFR. For the C04 sample, AGNs played a negligible role in the total X-ray emission from their galaxies and therefore all 24 late-type galaxies (i.e., spirals and irregulars) are included here. For the LIRG sample, the AGNs were identified following the techniques in Section 4.2; the remaining 13 “normal” LIRGs are members of the full *Chandra* sample. For the Iw09 sample of 44 LIRGs/ULIRGs, we excluded the 15 obvious AGNs noted by Iw09. We note, however, that Iw09 utilized X-ray hardness and/or the presence of a strong Fe K line at ≈ 6.4 keV to identify AGN activity in their LIRGs/ULIRGs, which is somewhat different from the methods used for our LIRG sample (see Section 4.2). For example, Arp 299, the only galaxy present in both the Iw09 LIRGs/ULIRGs and our LIRG sample, was classified as an AGN by Iw09; hereafter, we adopt our “normal galaxy” classification and physical properties for this source. For the remaining 29 “normal” LIRGs/ULIRGs from the Iw09 sample, 23 had estimates of M_* and SFR from H10, and for the six galaxies without H10 counterparts, we utilized the methods described in Section 2.2 to calculate M_* and SFR. In total, our full *Chandra* sample consists of 66 normal galaxies (i.e., 24 from C04, 13 LIRGs from this study, and 29 LIRGs/ULIRGs from Iw09) and we use these galaxies in the statistical analyses that follow.

5.1. A Chandra Perspective on the X-ray/SFR Correlation

In Figure 4(a), we show the galaxy-wide 2–10 keV luminosity $L_{\text{HX}}^{\text{gal}}$ versus SFR for the full *Chandra* sample. Beginning with a simple constant $L_{\text{HX}}^{\text{gal}}/\text{SFR}$ model, $\log L_{\text{HX}}^{\text{gal}}/\text{SFR} = A$, where A is a constant, we utilized the Kaplan–Meier estimator (e.g., Feigelson & Nelson 1985) available through the Astronomy SURVival Analysis software package (ASURV Rev. 1.2; Isobe & Feigelson 1990; LaValley et al. 1992) to calculate the mean logarithmic ratio A . The Kaplan–Meier estimator appropriately handles the censored data (i.e., $L_{\text{HX}}^{\text{gal}}$ upper limits) in our sample. We find $A = 39.24 \pm 0.06$ (in logarithmic units of $\text{erg s}^{-1} (M_{\odot} \text{ yr}^{-1})^{-1}$; 1σ error) with a 1σ scatter of 0.48 dex; this relation is plotted in Figure 4(a) with a dashed line and is tabulated in Table 4. Assuming a power-law scenario where $\log L_{\text{HX}}^{\text{gal}} = B + C \log \text{SFR}$, we utilized the expectation-maximization (EM) algorithm available through ASURV to find a best-fit relation of $B = 39.46 \pm 0.06$ and $C = 0.76 \pm 0.04$ (see Figure 4(a), dotted curve and Table 4). We note that the use of a power-law scenario reduces the scatter by ≈ 0.1 dex (≈ 0.39 dex scatter); however, the assumption of such a highly nonlinear relation over the entire SFR range is difficult to explain on physical grounds.

We note that at $\text{SFR} \gtrsim 1\text{--}10 M_{\odot} \text{ yr}^{-1}$, the slope of the X-ray/SFR relation appears to become flatter. Grimm et al. (2003) and Gilfanov et al. (2004a, 2004b) argue that such a change in slope is expected in a scenario where the X-ray emission is dominated by HMXBs and a universal HMXB luminosity function with a normalization that scales linearly

⁹ Feigelson et al. (2000) are available on the Web at <http://www.astro.psu.edu/xray/acis/memos/memoinde.html>

Table 4
Best-Fit X-ray/SFR Relations

Model Description	Best-Fit Parameters	1 σ Scatter (dex)
$\log L_{\text{HX}}^{\text{gal}} = A + \log \text{SFR}$	$A = 39.24 \pm 0.06$	0.48
$\log L_{\text{HX}}^{\text{gal}} = B + C \log \text{SFR}$	$B = 39.46 \pm 0.06$ and $C = 0.76 \pm 0.04$	0.39
$\log L_{\text{HX}}^{\text{gal}} = B + C \log \text{SFR}$ ($\text{SFR} \lesssim 0.4 M_{\odot} \text{ yr}^{-1}$)	$B = 39.57 \pm 0.11$ and $C = 0.94 \pm 0.15$	0.41
$\log L_{\text{HX}}^{\text{gal}} = B + C \log \text{SFR}$ ($\text{SFR} \gtrsim 0.4 M_{\odot} \text{ yr}^{-1}$)	$B = 39.49 \pm 0.21$ and $C = 0.74 \pm 0.12$	0.36
$L_{\text{HX}}^{\text{gal}} = \alpha M_{\star} + \beta \text{SFR}$	$\alpha = (9.05 \pm 0.37) \times 10^{28} \text{ erg s}^{-1} M_{\odot}^{-1}$ $\beta = (1.62 \pm 0.22) \times 10^{39} \text{ erg s}^{-1} (M_{\odot} \text{ yr}^{-1})^{-1}$	0.34

Notes. Summary of best-fit relations between $L_{\text{HX}}^{\text{gal}}$, SFR, and M_{\star} for the models described in Section 5. Fits have been performed following the methods described in Sections 5.1 and 5.2; all quoted errors are 1 σ . We note that the inclusion of both SFR and M_{\star} in the final model provides the least statistical scatter of all the models.

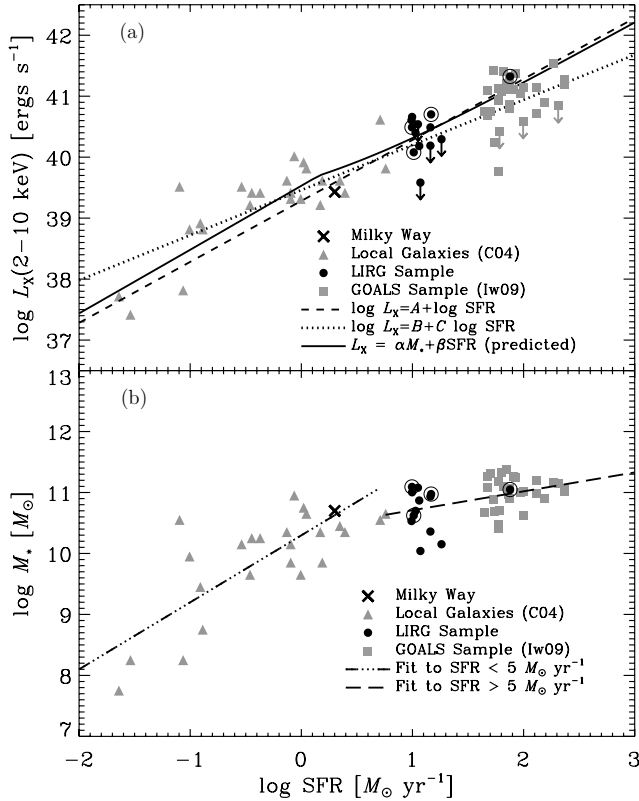


Figure 4. (a) Galaxy-wide 2–10 keV luminosity $L_{\text{HX}}^{\text{gal}}$ vs. SFR for the full *Chandra* sample: nearby normal galaxies from C04 (gray triangles), LIRGs from this study (black circles), and LIRGs/ULIRGs from the Iw09 GOALS study (gray squares) are plotted. We have highlighted “normal” LIRGs in our sample that show some evidence for AGN activity (see Column 10 of Table 3) with open circles. For reference, we have plotted the location of the MW as a cross. We have plotted the mean value of $\log L_{\text{HX}}^{\text{gal}}/\text{SFR}$ as a dashed line and our best-fit relation assuming a power law with $\log L_{\text{HX}}^{\text{gal}} = B + C \log \text{SFR}$ as a dotted line. The expected SFR-variable relation is plotted as a solid curve; this relation was derived using our best-fit relation for $L_{\text{HX}}^{\text{gal}} = \alpha M_{\star} + \beta \text{SFR}$ and the relationship between M_{\star} and SFR for galaxies with SFR and M_{\star} plotted in Figure 4(b). We note that this curve predicts well the general trend for the X-ray emission per SFR and tends to decrease with increasing SFR beyond $\text{SFR} \approx 1\text{--}10 M_{\odot} \text{ yr}^{-1}$. (b) M_{\star} vs. SFR for the full *Chandra* sample; symbols have the same meaning as they did in Figure 4(a). The dot-dashed and long-dashed curves highlight the best-fit relationship between M_{\star} and SFR for galaxies with $\text{SFR} \lesssim 5 M_{\odot} \text{ yr}^{-1}$ and $\text{SFR} \gtrsim 5 M_{\odot} \text{ yr}^{-1}$, respectively. We observe that for nearby galaxies with $\text{SFR} \lesssim 5 M_{\odot} \text{ yr}^{-1}$, M_{\star} and SFR are roughly linearly proportional; however, at higher SFR values, M_{\star}/SFR becomes smaller with increasing SFR.

with SFR is applied. In this scenario, at $\text{SFR} \lesssim 1\text{--}10 M_{\odot} \text{ yr}^{-1}$, the relation is expected to be steeper than linear ($L_{\text{HX}}^{\text{gal}} \propto \text{SFR}^{1.7}$), and at $\text{SFR} \gtrsim 1\text{--}10 M_{\odot} \text{ yr}^{-1}$, the relation is expected to become

linear ($L_{\text{HX}}^{\text{gal}} \propto \text{SFR}$). Dividing our data into low- and high-SFR regimes around $\text{SFR} = 5 M_{\odot} \text{ yr}^{-1}$ and performing power-law fits, we find

$$L_{\text{HX}}^{\text{gal}} = \begin{cases} 10^{(39.57 \pm 0.11)} \text{SFR}^{(0.94 \pm 0.15)} & \text{SFR} \lesssim 0.4 M_{\odot} \text{ yr}^{-1} \\ 10^{(39.49 \pm 0.21)} \text{SFR}^{(0.74 \pm 0.12)} & \text{SFR} \gtrsim 0.4 M_{\odot} \text{ yr}^{-1}, \end{cases}$$

where the cutoff $\text{SFR} \approx 0.4 M_{\odot} \text{ yr}^{-1}$ was determined by setting the upper and lower relations for $L_{\text{HX}}^{\text{gal}}$ equal to each other and solving for SFR. This two-regime relation can be used to obtain a reasonable estimate (with a 1 σ scatter of ≈ 0.4 dex; see Table 4) of $L_{\text{HX}}^{\text{gal}}$ based on SFR alone; however, as we will discuss in Section 6.2, some LIRGs and ULIRGs may fall $\approx 0.5\text{--}1$ dex below this relation due to significant intrinsic attenuation of the 2–10 keV emission. We note that the measured slopes of these relations are inconsistent with those predicted by Grimm et al. (2003) and Gilfanov et al. (2004a, 2004b). We speculate that this is due to the presence of LMXBs that provide a non-negligible contribution to $L_{\text{HX}}^{\text{gal}}$ in the low-SFR regime. In the next section, we explore the use of a physically motivated scaling of $L_{\text{HX}}^{\text{gal}}$ with M_{\star} and SFR that incorporates emission from both HMXB and LMXB populations.

5.2. Correlating $L_{\text{HX}}^{\text{gal}}$ with M_{\star} and SFR

From Figure 4(a), we notice that the mean $L_{\text{HX}}^{\text{gal}}/\text{SFR}$ ratio (dashed line) for the total *Chandra* sample generally lies below the data for galaxies with $\text{SFR} \lesssim 5 M_{\odot} \text{ yr}^{-1}$ (i.e., from C04), primarily due to the lower values of $L_{\text{HX}}^{\text{gal}}/\text{SFR}$ for the many LIRGs/ULIRGs in the sample. This trend has been noted by PR07, who suggest that typical nearby galaxies ($\text{SFR} \lesssim 5 M_{\odot} \text{ yr}^{-1}$) will have fractionally important contributions from both HMXBs and LMXBs, making them more X-ray luminous per unit SFR than “star formation active” galaxies like LIRGs/ULIRGs, which are likely to have negligible contributions from LMXBs and will be dominated by HMXBs. As recognized by C04, the total 2–10 keV luminosity for nearby galaxies can reasonably be quantified as the sum of contributions from LMXBs and HMXBs, which to first order are expected to scale linearly with M_{\star} and SFR, respectively.¹⁰ The C04 relation can be expressed using the following equation:

$$L_{\text{HX}}^{\text{gal}} = L_{\text{HX}}^{\text{gal}}(\text{LMXB}) + L_{\text{HX}}^{\text{gal}}(\text{HMXBs}) = \alpha M_{\star} + \beta \text{SFR}, \quad (3)$$

where α and β are scaling constants (see below). From Equation (3), we expect that galaxies with larger SFR/M_{\star}

¹⁰ However, see Grimm et al. (2003), Gilfanov et al. (2004a), and Gilfanov (2004) for different scalings depending on M_{\star} and SFR regimes.

will have more significant contributions from HMXBs, whereas galaxies with smaller SFR/M_* will have larger contributions from LMXBs. We would therefore expect that $L_{\text{HX}}^{\text{gal}}$ should scale more closely with SFR/M_* than SFR alone.

In Figure 4(b), we show M_* versus SFR for the full *Chandra* sample. It is apparent that there is a strong correlation between M_* and SFR (Spearman's ρ probability of $>99.99\%$). Using simple polynomial fitting techniques, we find for galaxies with $\text{SFR} \lesssim 5 M_\odot \text{ yr}^{-1}$, M_* and SFR are nearly linearly correlated ($M_* \propto \text{SFR}^{1.10}$); however, for galaxies with $\text{SFR} \gtrsim 5 M_\odot \text{ yr}^{-1}$, the relationship becomes shallower ($M_* \propto \text{SFR}^{0.27}$). From this analysis, we find that the quantity SFR/M_* remains roughly constant for $\text{SFR} \approx 0.01\text{--}1 M_\odot \text{ yr}^{-1}$, and to first order, this plausibly suggests that the HMXB and LMXB fractional contributions would remain roughly constant as well. Indeed, as noted in Section 5.1, we found that $L_{\text{HX}}^{\text{gal}} \propto \text{SFR}^{(0.94 \pm 0.15)}$ over this range of SFR. At $\text{SFR} \gtrsim 5 M_\odot \text{ yr}^{-1}$, the average SFR/M_* increases from a constant value, which would qualitatively allow for HMXBs to make an increasingly large fractional contribution to the total X-ray luminosity while the $L_{\text{HX}}^{\text{gal}}/\text{SFR}$ ratio decreases due to the reduced fractional contribution from LMXBs; in Section 5.1, we found that $L_{\text{HX}}^{\text{gal}} \propto \text{SFR}^{(0.74 \pm 0.12)}$ in this regime.

The best estimates to date of the quantities α and β come from the C04 analysis, which does not include *Chandra* constraints on galaxies with $\text{SFR} \gtrsim 5 M_\odot \text{ yr}^{-1}$ (i.e., LIRGs and ULIRGs), a regime where the SFR/M_* is expected to be large and HMXBs are likely to dominate. Here, we utilize the full *Chandra* sample to improve the calibration of α and β for data covering the broad range of $\text{SFR} \approx 0.01\text{--}400 M_\odot \text{ yr}^{-1}$.

Considering the above discussion, it is useful to examine the relationship of $L_{\text{HX}}^{\text{gal}}/\text{SFR}$ as a function of SFR/M_* . Following Equation (3), the quantity $L_{\text{HX}}^{\text{gal}}/\text{SFR}$ can be written as follows:

$$L_{\text{HX}}^{\text{gal}}/\text{SFR} = (\alpha M_* + \beta \text{SFR})/\text{SFR} = \alpha(\text{SFR}/M_*)^{-1} + \beta. \quad (4)$$

From Equation (4), we see that $L_{\text{HX}}^{\text{gal}}/\text{SFR} \propto (\text{SFR}/M_*)^{-1}$, and in Figure 5(a), we plot $L_{\text{HX}}^{\text{gal}}/\text{SFR}$ versus SFR/M_* for the full *Chandra* sample. We see that the IMF and X-ray bandpass adjusted C04 relation (dot-dashed curve in Figure 5(a)), which was determined solely from the C04 data (triangles), predicts well the basic observed trend; however, it mildly underpredicts $L_{\text{HX}}^{\text{gal}}/\text{SFR}$ for LIRGs and ULIRGs. Using the full *Chandra* sample, we fit the data using the EM algorithm and the model provided in Equation (4). We find best-fit values of $\alpha = (9.05 \pm 0.37) \times 10^{28} \text{ erg s}^{-1} M_\odot^{-1}$ and $\beta = (1.62 \pm 0.22) \times 10^{39} \text{ erg s}^{-1} (M_\odot \text{ yr}^{-1})^{-1}$ with a scatter of 0.34 dex, which is smaller than that produced by fitting for SFR alone (see Section 5.1; Table 4).

Our best-fit relation is plotted as a solid curve in Figure 5(a). In Figure 4(a), we combine this relation with the M_* –SFR relations provided in Section 5.1 and Figure 4(b) to show the expected $L_{\text{HX}}^{\text{gal}}$ –SFR relation (see solid curve in Figure 4(a)); in general, the combined relations appear to fit the data better than a simple mean $\log L_{\text{HX}}^{\text{gal}}/\text{SFR}$ ratio and a less physically meaningful power-law relation (i.e., $\log L_{\text{HX}}^{\text{gal}} = B + C\text{SFR}$).

After accounting for differences in IMF and X-ray bandpass, we find that $\alpha/\alpha(\text{C04}) = 0.76$ and $\beta/\beta(\text{C04}) = 2.18$, suggesting that for a given SFR/M_* , HMXBs provide ≈ 2.9 times larger $L_{\text{X}}^{\text{gal}}$ contributions over LMXBs than previously reported. We further note that our best-fit relation has reduced the error bars for α and β by factors of ≈ 3.8 and ≈ 2.1 , respectively. We find that

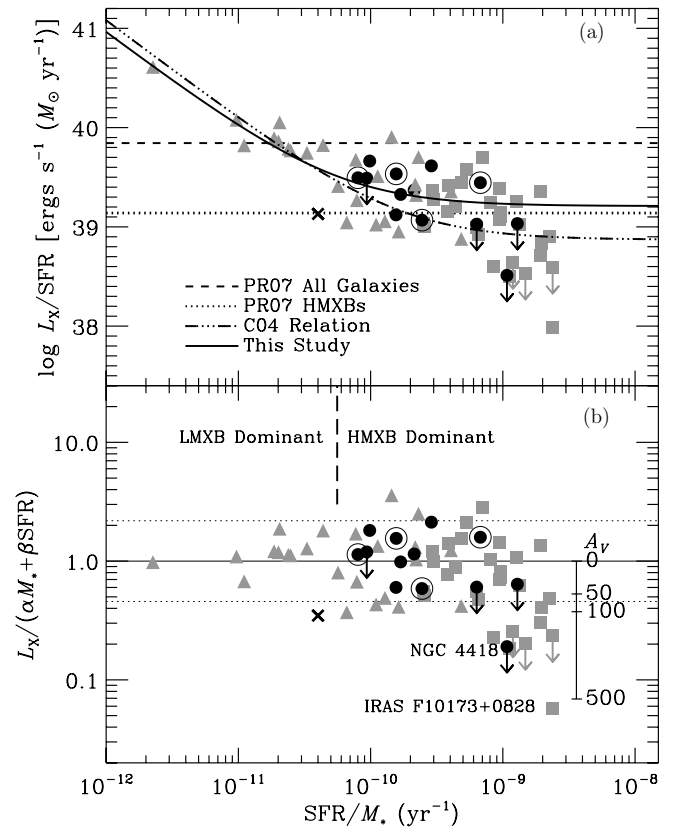


Figure 5. (a) Logarithm of the galaxy-wide 2–10 keV luminosity per SFR ($L_{\text{HX}}^{\text{gal}}/\text{SFR}$) vs. SFR/M_* for the full *Chandra* sample; symbols are the same as they were in Figure 4(a). The PR07 relations for all galaxies and HMXBs are shown as dashed and dotted lines, respectively. The C04 relation and our best-fit relation are shown as dash-dotted and solid curves, respectively. The clear dependence of $L_{\text{HX}}^{\text{gal}}/\text{SFR}$ on SFR/M_* convincingly illustrates that SFR plus M_* provides a superior estimate of $L_{\text{HX}}^{\text{gal}}$ than a simple $L_{\text{HX}}^{\text{gal}}/\text{SFR}$ correlation. (b) Residuals to the best-fit relation $L_{\text{HX}}^{\text{gal}} = \alpha M_* + \beta \text{SFR}$. Horizontal dotted lines show the 1σ scatter for this relation. We note that for the most star formation active galaxies, there are several sources that are X-ray underluminous; we have annotated the locations of NGC 4418 and IRAS F10173+0828, the most extreme outliers of the LIRGs and ULIRGs, respectively. For such sources, it is plausible that significant extinction ($A_V \gtrsim 50$ mag), which has been observed in powerful ULIRGs (see Section 6.2), will play a role in obscuring the 2–10 keV emission. For reference, we have plotted the expected attenuation of the 2–10 keV emission for optical extinction in the range of $A_V = 0\text{--}500$ mag (corresponding to $N_{\text{H}} \approx [0\text{--}1.2] \times 10^{24} \text{ cm}^{-2}$).

for $\text{SFR}/M_* \gtrsim 5.6 \times 10^{-11} \text{ yr}^{-1}$ (corresponding roughly to $\text{SFR} \gtrsim 2 M_\odot \text{ yr}^{-1}$ or $L_{\text{IR}} \gtrsim 2 \times 10^{10} L_\odot$ assuming the M_* –SFR correlation in Figure 4(b) and $\gamma = 1$ in Equation (2)), HMXBs will dominate the galaxy-wide 2–10 keV. This transition SFR/M_* is a factor of ≈ 2.9 times lower than previous estimates.

We note that the MW (plotted in Figure 5 as a cross) appears to be located below our best-fit correlation line by a factor of ≈ 0.37 dex, which is just outside the 1σ scatter in the relation. Our best-fit relation predicts that a galaxy with M_* and SFR equal to those of the MW, will have $L_{\text{HX}}^{\text{gal}}(\text{LMXB})/L_{\text{HX}}^{\text{gal}}(\text{HMXB}) \approx 1.4$, which is much less than the $L_{\text{HX}}^{\text{gal}}(\text{LMXB})/L_{\text{HX}}^{\text{gal}}(\text{HMXB}) \sim 10$ estimated by Grimm et al. (2002) using the measured luminosity functions of LMXBs and HMXBs. We speculate that these differences are due to either (1) the large uncertainties in measuring M_* and SFR for the MW, as a result of our location within it, and/or (2) the MW being a true outlier to the general correlation. It has been noted by Hammer et al.

(2007) that the MW does not appear to follow other correlations along physical parameter planes (e.g., planes drawn by disk rotation velocity, K -band luminosity, disk angular momentum, and mean $[\text{Fe}/\text{H}]$ abundances of stars in the outskirts of the disk) drawn using a sample of galaxies with similar M_* . Hammer et al. conclude that the MW is likely to have a different star formation history and disk construction than other similar galaxies; such conditions could plausibly affect the scaling of LMXB and HMXB power output with M_* and SFR, respectively.

6. DISCUSSION

In Figure 5(b), we show the residuals to our best-fit relation (i.e., $L_X/[\alpha M_* + \beta \text{SFR}]$). As noted in Section 5.2, the scatter over the entire range of SFR/M_* is ≈ 0.34 dex. There are several factors that are likely to contribute to the scatter in this relation including: (1) variations in the LMXB populations due to a diversity of stellar ages and star formation histories (e.g., Fragos et al. 2008); (2) unrelated low-level AGN activity that affects estimates of the X-ray and/or infrared luminosities, two quantities that are important to this analysis (e.g., Imanishi et al. 2007, 2010; Iw09); (3) strong statistical fluctuations due to small numbers of luminous X-ray binaries that dominate the total X-ray luminosity, particularly for galaxies with small SFR and/or M_* (e.g., Grimm et al. 2003; Gilfanov et al. 2004a; see Section 6.1); and (4) significant extinction that can affect estimates of stellar mass, and in the most extreme cases, may obscure even 2–10 keV emission (see Section 6.2). In Sections 6.1 and 6.2, we explore in more detail points (3) and (4), respectively.

6.1. Statistical Considerations at Low SFR and M_*

As discussed in Section 5.1, the qualitative change in slope of the X-ray/SFR correlation has previously been noted by Grimm et al. (2003) and Gilfanov et al. (2004a, 2004b) who predict such behavior for an HMXB-dominant $L_{\text{HX}}^{\text{gal}}$. These authors suggest that since the HMXB luminosity function is a relatively shallow power law with $dN/dL_{\text{XP}} \propto \text{SFR} L_{\text{XP}}^{-\gamma}$ (with $\gamma \approx 1.6$) and a maximum cutoff luminosity of $L_{\text{XP}}^{\text{cut-off}} \approx 2 \times 10^{40} \text{ erg s}^{-1}$ (see, e.g., Grimm et al. 2003; Swartz et al. 2004), then in the low-SFR regime, the most luminous HMXB will have a most probable luminosity $L_{\text{XP}}^{\text{max}} \propto \text{SFR}^{1/(\gamma-1)}$, which is less than $L_{\text{XP}}^{\text{cut-off}}$. In this regime, the integrated X-ray luminosity $L_{\text{HX}}^{\text{gal}}$ is therefore expected to scale with $\text{SFR}^{1/(\gamma-1)}$ (or $\text{SFR}^{1.7}$ in the case of $\gamma = 1.6$). Such an effect is predicted to produce a nonlinear SFR dependence for the HMXB contribution to $L_{\text{HX}}^{\text{gal}}$ for $\text{SFR} \lesssim 1\text{--}10 M_\odot \text{ yr}^{-1}$. Similar logic can be applied to the LMXB contribution to $L_{\text{HX}}^{\text{gal}}$ using the more complex luminosity function for LMXBs, which is expected to have a linear normalization that scales with M_* . However, the cutoff luminosity for the LMXB population is likely to be much lower ($\sim 10^{39} \text{ erg s}^{-1}$) than that of HMXBs and therefore $L_{\text{HX}}^{\text{gal}}(\text{LMXB})$ is expected to be linear for galaxies with $M_* \gtrsim 5\text{--}20 \times 10^9 M_\odot$ and very close to linear for smaller values of M_* (e.g., Gilfanov et al. 2004a; Gilfanov 2004).

In Section 5.1, we noted that in the low-SFR regime ($\text{SFR} \approx 0.01\text{--}1 M_\odot \text{ yr}^{-1}$), $L_{\text{HX}}^{\text{gal}}/\text{SFR}$ and SFR/M_* were roughly constant; over this range these quantities have median values of $\approx 5 \times 10^{39} \text{ erg s}^{-1} (M_\odot \text{ yr}^{-1})^{-1}$ and $8 \times 10^{-11} \text{ yr}^{-1}$, respectively. From our best-fit relation for Equation (3), we estimate $L_{\text{HX}}^{\text{gal}}(\text{LMXB})/L_{\text{HX}}^{\text{gal}}(\text{HMXB}) \approx 0.74$ for these galax-

ies, suggesting that both LMXBs and HMXBs are estimated to provide significant contributions to $L_{\text{HX}}^{\text{gal}}$ in this regime. However, if indeed $L_{\text{HX}}^{\text{gal}}(\text{HMXB}) \propto \text{SFR}^{1.7}$ and $L_{\text{HX}}^{\text{gal}}(\text{LMXB}) \propto M_* \propto \text{SFR}$ are accurate descriptions of the respective HMXB and LMXB emission in this regime, then we would have expected that $L_{\text{HX}}^{\text{gal}} \propto \text{SFR}^{1.0\text{--}1.7}$. In Section 5.1, we found that $L_{\text{HX}}^{\text{gal}} \propto \text{SFR}^{(0.94 \pm 0.15)}$. This suggests that either (1) $L_{\text{HX}}^{\text{gal}}(\text{HMXB})$ scales with $\text{SFR}^{1.7}$ and provides a small contribution to $L_{\text{HX}}^{\text{gal}}$ or (2) $L_{\text{HX}}^{\text{gal}}(\text{HMXB}) \propto \text{SFR}$. Future X-ray and multiwavelength studies of large numbers of normal galaxies in this regime may provide the necessary statistical basis to allow discrimination between these two scenarios; future X-ray missions such as the *International X-ray Observatory* (IXO) and *WFXT* will enable efficient detection of many galaxies in the low-SFR regime.¹¹ Otherwise, a combination of X-ray and optical/near-IR observatories with highly precise astrometry would be needed to allow for the detection of X-ray binaries and the reliable identification and classification of their stellar counterparts in external galaxies. This is currently broadly possible with the combination of *Chandra* and *HST* data for a small number of nearby galaxies. Future missions such as *Generation-X* and *James Webb Space Telescope* (JWST) will undoubtedly expand this science to more representative galaxies that cover the entire low-SFR regime.¹²

6.2. A Deficit of X-ray Emission in the Most Actively Star-Forming Galaxies

From Figure 5(b), it is evident that for several of the most star formation active LIRGs/ULIRGs (i.e., $\text{SFR}/M_* \gtrsim 10^{-9} \text{ yr}^{-1}$) in the total *Chandra* sample there is a departure from the best-fit relation. For example, IRAS 07251–0248, IRAS F15250+3608, IRAS F10173+0828, IRAS 21101+5810, and NGC 4418 all have residuals to our best fit that fall below the 2σ scatter, when only $\approx 1\text{--}2$ galaxies are expected statistically over the entire SFR/M_* range. If we exclude galaxies with $\text{SFR}/M_* \gtrsim 10^{-9} \text{ yr}^{-1}$, this significantly reduces the scatter to ≈ 0.26 dex (i.e., by $\approx 20\%$). Studies of LIRGs/ULIRGs have found that in these objects the powerful star formation activity occurs in compact regions that are surrounded by large columns of gas and dust (e.g., Soifer et al. 2000; Alonso-Herrero et al. 2006b; Siebenmorgen et al. 2008). The obscuration to these star-forming regions can be very significant ($A_V \gtrsim 50 \text{ mag}$; e.g., Genzel et al. 1998; Siebenmorgen & Krügel 2007) and can attenuate emission over the 2–10 keV bandpass.

To estimate the effect that obscuration can have on the observed 2–10 keV power for ULIRG levels of extinction, we first converted A_V to N_{H} following the relation $N_{\text{H}} \approx 2.3 \times 10^{21} A_V \text{ cm}^{-2}$ from Güver & Özel (2009), which was calibrated using measurements of various columns through the MW. We note that this calibration has been calibrated only over the range of $A_V \approx 0.2\text{--}30 \text{ mag}$ and is subject to large uncertainties when applied to other galaxies, which may have different chemical compositions in their interstellar mediums. A range of $A_V = 0\text{--}500$ therefore implies column densities in the range $N_{\text{H}} \approx 0\text{--}1.2 \times 10^{24} \text{ cm}^{-2}$. Using PIMMS and an assumed power-law X-ray spectral energy distribution (SED) with $\Gamma = 1.8$, we find that the emergent 2–10 keV luminosity

¹¹ More information regarding IXO and WFXT can be found at <http://ixo.gsfc.nasa.gov/> and <http://wfxt.pha.jhu.edu/>, respectively.

¹² More information regarding Generation-X and JWST can be found at <http://www.cfa.harvard.edu/hea/genx/> and <http://www.jwst.nasa.gov/>, respectively.

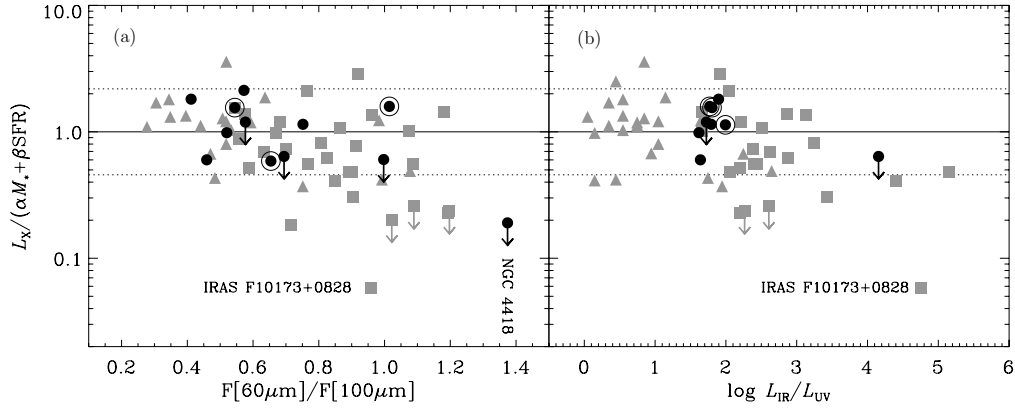


Figure 6. Residuals to the best-fit relation $L_{\text{HX}}^{\text{gal}} = \alpha M_{\star} + \beta \text{SFR}$ vs. the *IRAS* 60–100 μm flux density ratio F_{60}/F_{100} (a) and the logarithm of the infrared-to-UV luminosity ratio $\log L_{\text{IR}}/L_{\text{UV}}$ (b). Symbols and lines have the same meaning as they did in Figure 5(b). A Spearman’s ρ test reveals that the residuals are negatively correlated with F_{60}/F_{100} and $\log L_{\text{IR}}/L_{\text{UV}}$ at the $\approx 99.8\%$ and 99.9% confidence levels, respectively. The quantity F_{60}/F_{100} is a proxy for temperature and infrared luminosity density (star formation density) and $\log L_{\text{IR}}/L_{\text{UV}}$ is a direct measure of UV obscuration. These relations suggest that the most X-ray deficient LIRGs and ULIRGs, which have relatively warm dust temperatures and large UV obscuration due to dust, contain dense buried star-forming regions with attenuated 2–10 keV emission.

will be attenuated by factors of ≈ 2 , 3, and 15 for $A_V \approx 50$, 100, and 500, respectively (see vertical bar in Figure 5(b)); such visual extinctions are likely to be present in at least some LIRGs/ULIRGs (e.g., Genzel et al. 1998 estimate that some ULIRGs may even reach $A_V \approx 1000$). We note that there are only a few LIRGs/ULIRGs in our sample with the high-quality optical to far-IR data required to estimate A_V accurately. For example, the well-studied ULIRG Arp 220 has a 2–10 keV luminosity that is a factor of ≈ 3 times lower than that expected from our best-fit relation for Equation (4). Detailed modeling of the infrared-to-optical spectrum suggests a global value of $A_V \approx 50$ –150 mag (e.g., Siebenmorgen & Krügel 2007), implying $N_{\text{H}} \approx (1.2$ – $3.5) \times 10^{23} \text{ cm}^{-2}$ and therefore an expected factor of ≈ 2 –4 attenuation of the intrinsic 2–10 keV luminosity, in good agreement with the deficit that we observe.

To assess whether there is broader evidence that the X-ray underluminous LIRGs/ULIRGs in the full *Chandra* sample may be subject to significant 2–10 keV attenuation, we utilized two informative quantities: (1) the *IRAS* 60–100 μm flux ratio (F_{60}/F_{100}), which has been shown to correlate well with mean dust temperature and infrared luminosity surface density (e.g., Chanial et al. 2007) and (2) the IR-to-UV luminosity ratio ($L_{\text{IR}}/L_{\text{UV}}$), which provides a direct measure of UV obscuration from star-forming regions. If the X-ray emission from star-forming regions is buried under significant absorbing columns, we would expect the star formation to be highly concentrated and not dispersed through the galaxy (i.e., large F_{60}/F_{100}) and heavily obscured in the UV (i.e., large $L_{\text{IR}}/L_{\text{UV}}$). In Figures 6(a) and (b), we plot the residuals to our best-fit relation ($L_{\text{HX}}^{\text{gal}}/[\alpha M_{\star} + \beta \text{SFR}]$) versus F_{60}/F_{100} and $L_{\text{IR}}/L_{\text{UV}}$, respectively. It is evident that the LIRGs/ULIRGs with the largest deficit of X-ray emission with respect to our best-fit relation are those with large values of F_{60}/F_{100} and $L_{\text{IR}}/L_{\text{UV}}$; a Spearman’s ρ test reveals that the residuals are correlated with each quantity at the 99.8% and 99.9% significance levels, respectively. We therefore conclude that obscuration is at least partially responsible for the deficit of observed 2–10 keV emission at the largest SFR/ M_{\star} .

7. CONCLUSIONS

In this paper, we present new results from *Chandra* observations of a complete sample of 17 LIRGs with $D < 60$ Mpc

and Galactic column densities $N_{\text{H}} \lesssim 5 \times 10^{20} \text{ cm}^{-2}$. Our *Chandra* observations reveal a variety of X-ray morphologies for the LIRGs, with the majority of their corresponding X-ray spectra being well-described by a hot-gas component (with $kT \lesssim 0.8$ keV) plus a power law ($\Gamma \approx 1$ –3), which is expected to originate from X-ray binaries, and when present, an AGN. We find that 4 out of the 17 LIRGs both show evidence for AGN activity in the optical, infrared, and/or X-ray band and contain a nuclear component that dominates the integrated 2–10 keV luminosity. We study the galaxy-wide 2–10 keV luminosity $L_{\text{HX}}^{\text{gal}}$ and its correlation with SFR and M_{\star} using the 13 non-AGN-dominant LIRGs combined with *Chandra* studies of less star formation active normal galaxies (from C04) and more powerful LIRGs and ULIRGs (from Iw09), collectively referred to as the total *Chandra* sample. Our key results can be summarized as follows.

1. For the galaxies that make up our total *Chandra* sample, we find that SFR and M_{\star} are strongly correlated, such that $M_{\star} \propto \text{SFR}^{1.10}$ for $\text{SFR} \approx 0.01$ – $5 M_{\odot} \text{ yr}^{-1}$ and $M_{\star} \propto \text{SFR}^{0.27}$ for $\text{SFR} \gtrsim 5 M_{\odot} \text{ yr}^{-1}$ (see Figure 4(b)).
2. We find that $L_{\text{HX}}^{\text{gal}}$ is strongly correlated with SFR (the X-ray/SFR correlation), as has been found in previous studies (see Figure 4(b)). Similar to point (1), the X-ray/SFR correlation slope becomes shallower for $\text{SFR} \gtrsim 1$ – $10 M_{\odot} \text{ yr}^{-1}$. We find that $L_{\text{HX}}^{\text{gal}} = (39.57 \pm 0.11) \text{SFR}^{(0.94 \pm 0.15)}$ for $\text{SFR} \lesssim 0.4 M_{\odot} \text{ yr}^{-1}$ and $L_{\text{HX}}^{\text{gal}} = (39.49 \pm 0.21) \text{SFR}^{(0.74 \pm 0.12)}$ for $\text{SFR} \gtrsim 0.4 M_{\odot} \text{ yr}^{-1}$ provides a reasonable (with ≈ 0.4 dex scatter; see Table 4) estimate of the $L_{\text{HX}}^{\text{gal}}$. The change in slope is likely to be related to the changing slope of the correlation between SFR and M_{\star} , since we expect the total galaxy-wide 2–10 keV luminosity to be the sum of contributions from HMXBs and LMXBs, which to first order are expected to scale with SFR and M_{\star} , respectively.
3. Under the assumption that $L_{\text{HX}}^{\text{gal}}$ can be written as $L_{\text{HX}}^{\text{gal}} = L_{\text{HX}}^{\text{gal}}(\text{LMXB}) + L_{\text{HX}}^{\text{gal}}(\text{HMXB}) = \alpha M_{\star} + \beta \text{SFR}$, we find best-fitting parameters of $\alpha = (9.05 \pm 0.37) \times 10^{28} \text{ erg s}^{-1} M_{\odot}^{-1}$ and $\beta = (1.62 \pm 0.22) \times 10^{39} \text{ erg s}^{-1} (M_{\odot} \text{ yr}^{-1})^{-1}$. These values suggest that HMXBs dominate the X-ray emission for $\text{SFR}/M_{\star} \gtrsim 5.9 \times 10^{-11} \text{ yr}^{-1}$, a factor of ≈ 2.9 times lower than previous estimates.

4. For the most actively star-forming LIRGs and ULIRGs (i.e., those with $\text{SFR}/M_{\star} \gtrsim 10^{-9} \text{ yr}^{-1}$), we find an excess of objects with $L_{\text{HX}}^{\text{gal}}$ lower than expected. These sources have infrared colors and UV to total-IR luminosities indicative of compact star-forming regions with extreme extinction. We argue that such star-forming regions are likely to have attenuated 2–10 keV emission.

We thank the referee for helpful comments that have improved the manuscript. We thank Kazushi Iwasawa for generously sharing data and Lee Armus and Joseph Mazzarella for helpful discussions. We gratefully acknowledge financial support from the Einstein Fellowship Program (B.D.L.), the Royal Society (D.M.A.), the Leverhulme Trust (D.M.A.), *Chandra* X-ray Center grants G09-0134A (W.N.B.) and G09-0134B (F.E.B.), and NASA ADP grant NNX10AC99G (W.N.B.). This research has made use of the NASA/IPAC Extragalactic Database (NED), which is operated by the Jet Propulsion Laboratory, California Institute of Technology, under contract with NASA.

REFERENCES

- Alonso-Herrero, A., Colina, L., Packham, C., Díaz-Santos, T., Rieke, G. H., Radomski, J. T., & Telesco, C. M. 2006a, *ApJ*, **652**, L83
- Alonso-Herrero, A., Rieke, G. H., Rieke, M. J., Colina, L., Pérez-González, P. G., & Ryder, S. D. 2006b, *ApJ*, **650**, 835
- Alonso-Herrero, A., et al. 2009, *ApJ*, **697**, 660
- Armus, L., Heckman, T. M., & Miley, G. K. 1989, *ApJ*, **347**, 727
- Armus, L., et al. 2009, *PASP*, **121**, 559
- Arnaud, K. A. 1996, in ASP Conf. Ser. 101, *Astronomical Data Analysis Software and Systems V*, ed. G. Jacoby & J. Barnes (San Francisco, CA: ASP), 17
- Baan, W. A., Salzer, J. J., & Lewinter, R. D. 1998, *ApJ*, **509**, 633
- Bauer, F. E., Alexander, D. M., Brandt, W. N., Hornschemeier, A. E., Vignali, C., Garmire, G. P., & Schneider, D. P. 2002, *AJ*, **124**, 2351
- Bauer, F. E., Alexander, D. M., Brandt, W. N., Schneider, D. P., Treister, E., Hornschemeier, A. E., & Garmire, G. P. 2004, *AJ*, **128**, 2048
- Bell, E. F., McIntosh, D. H., Katz, N., & Weinberg, M. D. 2003, *ApJS*, **149**, 289
- Bell, E. F., et al. 2005, *ApJ*, **625**, 23
- Cash, W. 1979, *ApJ*, **228**, 939
- Chañal, P., Flores, H., Guiderdoni, B., Elbaz, D., Hammer, F., & Vigroux, L. 2007, *A&A*, **462**, 81
- Chen, Y., Lowenthal, J. D., & Yun, M. S. 2010, *ApJ*, **712**, 1385
- Colbert, E. J. M., Heckman, T. M., Ptak, A. F., Strickland, D. K., & Weaver, K. A. 2004, *ApJ*, **602**, 231 (C04)
- Coziol, R., Torres, C. A. O., Quast, G. R., Contini, T., & Davoust, E. 1998, *ApJS*, **119**, 239
- de Vaucouleurs, G., de Vaucouleurs, A., Corwin, H. G., Buta, R. J., Paturel, G., & Fouque, P. 1991, *The Third Reference Catalogue of Bright Galaxies*. Vol. 1–3, XII (Berlin: Springer)
- Della Ceca, R., et al. 2002, *ApJ*, **581**, L9
- Dickey, J. M., & Lockman, F. J. 1990, *ARA&A*, **28**, 215
- Fabbiano, G. 1989, *ARA&A*, **27**, 87
- Fabbiano, G. 2006, *ARA&A*, **44**, 323
- Feigelson, E. D., & Nelson, P. I. 1985, *ApJ*, **293**, 192
- Feigelson, E., Broos, P., & Gaffney, J. 2000, <http://www.astro.psu.edu/xray/acis/memos/memoindex.html>
- Fragos, T., et al. 2008, *ApJ*, **683**, 346
- Franceschini, A., et al. 2003, *MNRAS*, **343**, 1181
- García-Marín, M., Colina, L., Arribas, S., Alonso-Herrero, A., & Mediavilla, E. 2006, *ApJ*, **650**, 850
- Genzel, R., et al. 1998, *ApJ*, **498**, 579
- Gilfanov, M. 2004, *MNRAS*, **349**, 146
- Gilfanov, M., Grimm, H.-J., & Sunyaev, R. 2004a, *MNRAS*, **351**, 1365
- Gilfanov, M., Grimm, H.-J., & Sunyaev, R. 2004b, *Nucl. Phys. B: Proc. Suppl.*, **132**, 369
- Goulding, A. D., & Alexander, D. M. 2009, *MNRAS*, **398**, 1165
- Grimm, H.-J., Gilfanov, M., & Sunyaev, R. 2002, *A&A*, **391**, 923
- Grimm, H.-J., Gilfanov, M., & Sunyaev, R. 2003, *MNRAS*, **339**, 793
- Güver, T., & Özel, F. 2009, *MNRAS*, **400**, 2050
- Hammer, F., Puech, M., Chemin, L., Flores, H., & Lehnert, M. D. 2007, *ApJ*, **662**, 322
- Hickox, R. C., & Markevitch, M. 2006, *ApJ*, **645**, 95
- Ho, L. C., Filippenko, A. V., & Sargent, W. L. W. 1997, *ApJS*, **112**, 315
- Hornschemeier, A. E., et al. 2001, *ApJ*, **554**, 742
- Howell, J. H., et al. 2010, *ApJ*, **715**, 572 (H10)
- Imanishi, M., Dudley, C. C., Maiolino, R., Maloney, P. R., Nakagawa, T., & Risaliti, G. 2007, *ApJS*, **171**, 72
- Imanishi, M., Maiolino, R., & Nakagawa, T. 2010, *ApJ*, **709**, 801
- Isobe, T., & Feigelson, E. 1990, *BAAS*, **22**, 917
- Iwasawa, K., Sanders, D. B., Evans, A. S., Mazzarella, J. M., Armus, L., & Surace, J. A. 2009, *ApJ*, **695**, L103 (Iw09)
- Jarrett, T. H., Chester, T., Cutri, R., Schneider, S. E., & Huchra, J. P. 2003, *AJ*, **125**, 525
- Jenkins, L. P., Roberts, T. P., Ward, M. J., & Zezas, A. 2005, *MNRAS*, **357**, 109
- Kaaret, P., & Alonso-Herrero, A. 2008, *ApJ*, **682**, 1020
- Keel, W. C., Kennicutt, R. C., Jr., Hummel, E., & van der Hulst, J. M. 1985, *AJ*, **90**, 708
- Kennicutt, R. C., Jr. 1998, *ARA&A*, **36**, 189
- Kennicutt, R. C., Jr., et al. 2003, *PASP*, **115**, 928
- Kewley, L. J., Heisler, C. A., Dopita, M. A., & Lumsden, S. 2001, *ApJS*, **132**, 37
- Kim, M., Wilkes, B. J., Kim, D.-W., Green, P. J., Barkhouse, W. A., Lee, M. G., Silverman, J. D., & Tananbaum, H. D. 2007, *ApJ*, **659**, 29
- Kroupa, P. 2001, *MNRAS*, **322**, 231
- Lavalley, M., Isobe, T., & Feigelson, E. 1992, in ASP Conf. Ser. 25, *Astronomical Data Analysis Software and Systems I*, ed. D. M. Worrall, C. Biemesderfer, & J. Barnes (San Francisco, CA: ASP), 245
- Lehmer, B. D., et al. 2008, *ApJ*, **681**, 1163
- Levenson, N. A., Weaver, K. A., Heckman, T. M., Awaki, H., & Terashima, Y. 2004, *ApJ*, **602**, 135
- McKee, C. F., & Williams, J. P. 1997, *ApJ*, **476**, 144
- Melnick, J., & Mirabel, I. F. 1990, *A&A*, **231**, L19
- Moretti, A., Campana, S., Lazzati, D., & Tagliaferri, G. 2003, *ApJ*, **588**, 696
- Ogle, P. M., Brookings, T., Canizares, C. R., Lee, J. C., & Marshall, H. L. 2003, *A&A*, **402**, 849
- Persic, M., & Rephaeli, Y. 2002, *A&A*, **382**, 843
- Persic, M., & Rephaeli, Y. 2007, *A&A*, **463**, 481
- Persic, M., Rephaeli, Y., Braitto, V., Cappi, M., Della Ceca, R., Franceschini, A., & Gruber, D. E. 2004, *A&A*, **419**, 849
- Ptak, A., Heckman, T., Levenson, N. A., Weaver, K., & Strickland, D. 2003, *ApJ*, **592**, 782
- Ranalli, P., Comastri, A., & Setti, G. 2003, *A&A*, **399**, 39
- Risaliti, G., et al. 2009a, *ApJ*, **696**, 160
- Risaliti, G., et al. 2009b, *ApJ*, **705**, L1
- Sandage, A., & Tammann, G. A. 1981, *Revised Shapley-Ames Catalog of Bright Galaxies* (Publ. 635; Washington, DC: Carnegie Inst.)
- Sanders, D. B., Mazzarella, J. M., Kim, D.-C., Surace, J. A., & Soifer, B. T. 2003, *AJ*, **126**, 1607
- Sanders, D. B., & Mirabel, I. F. 1996, *ARA&A*, **34**, 74
- Sanders, D. B., Soifer, B. T., Elias, J. H., Neugebauer, G., & Matthews, K. 1988, *ApJ*, **328**, L35
- Scoville, N. Z., et al. 2000, *AJ*, **119**, 991
- Siebenmorgen, R., & Krügel, E. 2007, *A&A*, **461**, 445
- Siebenmorgen, R., et al. 2008, *A&A*, **488**, 83
- Smith, D. A., & Wilson, A. S. 2003, *ApJ*, **591**, 138
- Soifer, B. T., et al. 2000, *AJ*, **119**, 509
- Soria, R., Risaliti, G., Elvis, M., Fabbiano, G., Bianchi, S., & Kuncic, Z. 2009, *ApJ*, **695**, 1614
- Spergel, D. N., et al. 2003, *ApJS*, **148**, 175
- Strateva, I. V., & Komossa, S. 2009, *ApJ*, **692**, 443
- Swartz, D. A., Ghosh, K. K., Tennant, A. F., & Wu, K. 2004, *ApJS*, **154**, 519
- Veilleux, S., Kim, D.-C., Sanders, D. B., Mazzarella, J. M., & Soifer, B. T. 1995, *ApJS*, **98**, 171
- Veron-Cetty, M.-P., & Veron, P. 1986, *A&AS*, **66**, 335
- Wang, J., Fabbiano, G., Elvis, M., Risaliti, G., Mazzarella, J. M., Howell, J. H., & Lord, S. 2009, *ApJ*, **694**, 718
- Young, A. J., Wilson, A. S., & Shopbell, P. L. 2001, *ApJ*, **556**, 6
- Yuan, T.-T., Kewley, L. J., & Sanders, D. B. 2010, *ApJ*, **709**, 884
- Zezas, A., Ward, M. J., & Murray, S. S. 2003, *ApJ*, **594**, L31